TU Delft

Delft University of Technology

Document Version
Final published version

Licence
Dutch Copyright Act (Article 25fa)

Citation (APA)
Bannenberg, L. J. (2026). Thin-film metal hydrides. In *Metal Hydrides for Hydrogen-Based Energy Storage: Applications* (Vol. 2, pp. 103-155). Elsevier. https://doi.org/10.1016/B978-0-443-44873-7.00050-3

Important note
To cite this publication, please use the final published version (if applicable).
Please check the document version above.

Copyright
In case the licence states “Dutch Copyright Act (Article 25fa)”, this publication was made available Green Open Access via the TU Delft Institutional Repository pursuant to Dutch Copyright Act (Article 25fa, the Taverne amendment). This provision does not affect copyright ownership.
Unless copyright is transferred by contract or statute, it remains with the copyright holder.

Sharing and reuse
Other than for strictly personal use, it is not permitted to download, forward or distribute the text or part of it, without the consent of the author(s) and/or copyright holder(s), unless the work is under an open content license such as Creative Commons.

Takedown policy
Please contact us and provide details if you believe this document breaches copyrights.
We will remove access to the work immediately and investigate your claim.

This work is downloaded from Delft University of Technology.

Thin-film metal hydrides

3

Lars J. Bannenberg
Delft University of Technology, Faculty of Applied Sciences, Delft, the Netherlands

3.1 Introduction

Motivated by scientific research, the high degree of control and variety in material synthesis, and promising applications, thin film metal hydrides have been widely studied. Although thin films do share many similarities with bulk materials, their thermodynamics can be substantially different. Naturally, the thin layers (5–1000 nm) in thin film materials have a much larger surface-to-volume ratio than bulk materials, implying that surface and interface effects have a much more pronounced influence. In addition, different from bulk materials, the 2D nature of thin films assures that thin films need to obey constraints when the absorption of hydrogen induces a volumetric expansion of the material which can lead to high in-plane stresses. Both the high in-plane stresses and additional surface/interface effects can result in the severely altered properties of thin film metal hydrides, including a reduction of the critical temperature, shifting of phase boundaries and extensions of solubility limits of hydrogen in the (original) host metal lattice. These effects can, when understood and applied correctly, be used to tailor the properties of metal hydrides in various applications (Baldi & Dam, 2011; Pundt & Kirchheim, 2006; Remhof & Borgschulte, 2008).

The 2D character of thin films also affects the equilibrium thermodynamics and enable much faster kinetics of the hydrogenation in thin films than in the bulk. This is the result of the much shorter diffusion lengths and the fact that thin film metal hydrides are often combined with thin catalyst layers. These catalyst layers aid the dissociation of the hydrogen molecule into two H atoms, which is required for hydrogen to be absorbed by the material. Palladium and its alloys, which enable hydrogen dissociation at (or below) room temperature, are typically the materials of choice, while at elevated temperatures platinum, nickel or ruthenium can also be used. These materials typically serve a dual purpose as they also prevent oxidation of the metal hydride layer underneath.

The large control over sample composition and thickness that can typically be achieved during thin film metal hydride synthesis, commonly performed by using magnetron sputtering, e-beam evaporation or pulsed laser deposition, also provide opportunities to scan and tailor the composition of materials. This has proven to be useful, especially in the search for the ultimate light-weight metal hydride hydrogen storage material for which thin films have often been applied as model systems. In this application, metal hydrides act as a storage medium for hydrogen by reversibly absorbing and desorbing hydrogen allowing to achieve much larger volumetric densities of hydrogen than when storing hydrogen as a liquid or pressurised gas. As such, one aims to find a material that can absorb and desorb H_2 under favourable (pressure/

Metal Hydrides for Hydrogen-Based Energy Storage, Volume 2: Applications
https://doi.org/10.1016/B978-0-443-44873-7.00050-3
Copyright © 2026 Elsevier Ltd. All rights are reserved, including those for text and data mining, AI training, and similar technologies.

temperature) conditions, with fast kinetics and over a large number of cycles. To find the ultimate material, magnetron co-deposition of thin films in combination with high-throughput analytical techniques to quickly determine relevant material properties such as plateau pressures, enthalpies and entropies of formation, hydrogen solubility and kinetics has been widely employed to quickly screen the materials. An example of such a combinatorial methodology is to employ optical transmission measurements (hydrogenography) that allow the study of either compositional/thickness gradient thin films or the simultaneous study of varying hydride compositions at once.

Apart from the storage of hydrogen, thin film metal hydrides are also considered for switchable mirrors and as hydrogen sensing materials. Both applications are making use of profound optical changes that occur in some metal hydrides when (more) hydrogen is absorbed. First discovered in the mid-nineties for the lanthanum and yttrium hydrides, a metal-to-insulator transition occurs when e.g., LaH_2 absorbs hydrogen and transforms to LaH_3. Such a reversible transition can be used for the smart window applications, where the window can be made transparent or reflective, significantly reducing the heating/cooling costs of a building.

The structure of this chapter is as follows. First, we will discuss the thermodynamics of thin film metal hydrides. Next, we consider two methodologies dedicated to the thin film metal hydride research and widely used for the study of thin film metal hydrides: X-ray/neutron reflectometry and optical transmission measurements (hydrogenography). Thereafter, we consider three main applications of thin film metal hydrides: hydrogen storage materials, switchable mirrors, and hydrogen sensors.

3.2 Thermodynamics of thin film metal hydrides

3.2.1 Basic thermodynamics of metal hydrides

Similar to bulk metals, thin films metals form metal hydrides during their hydrogenation:

$$M + \frac{x}{2}H_2 \leftrightarrow MH_x \tag{3.1}$$

where M is a metal and x is the hydrogen-to-metal ratio. The relationship between the partial hydrogen pressure and and hydrogen-to-metal ratio at a certain temperature is described by a Pressure-Composition-Isotherm (PCI) of which some examples are provided in Fig. 3.1. In this Figure, the archetype metal hydride phase diagram is also presented that shows strong similarities with the phase diagrams of palladium and magnesium. We note that for many transition metals in particular for vanadium, tantalum and niobium, the phase diagrams are considerably more complex.

Fig. 3.1 illustrates that for low hydrogen pressures, hydrogen forms a solid solution with the metallic host lattice and the hydrogen atoms e.g., the hydrogen atoms reside at the tetrahedral or octahedral interstitial sites. This phase is what is often referred to as an 'α-phase'. The exact solubility of hydrogen in the α-phase can typically for low x

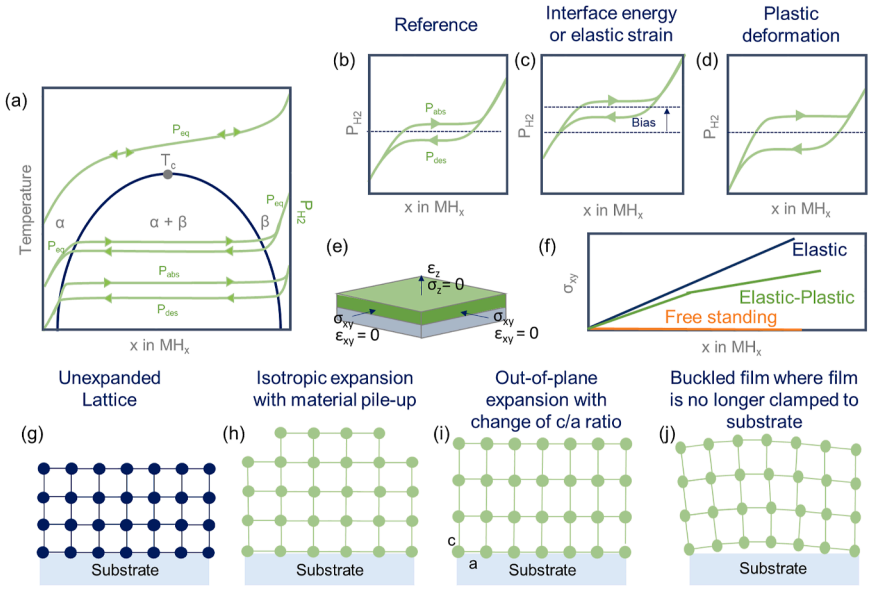


Figure 3.1 Thermodynamics of thin film metal hydrides. (a) Typical hydrogen-to-metal ratio x – temperature – partial hydrogen pressure P_{H2}- metal hydride phase diagram. In the diagram, several pressure-composition-isotherm (PCIs) are illustrated. These are curves indicating the hydrogen-to-metal ratio at a given partial hydrogen pressure and for a constant temperature. Note that the PCIs can be different for increasing and decreasing pressures, in which case we speak of hysteresis. At low partial hydrogen pressures, the α-phase exists, a solid solution of hydrogen atoms with the host metal lattice of which x depends on the partial hydrogen pressure. At the plateau pressure, P_{plat}, the β-phase starts to nucleate and grows at the expense of the α-phase at a constant pressure. The β-phase is a high-hydrogen concentration (metal hydride) phase. For $P_{H2} > P_{plat}$ the hydrogen-to-metal ratio will increase in the β-phase. The PCIs shift with increasing temperature to higher pressures. Above the critical temperature $T_{C,}$ no phase transition and plateau pressure are observed, and hydrogen forms a solid solution with the host metal over the entire hydrogen-to-metal ratio range. (b)–(d) Schematic illustrations how interface energy and other thermodynamic biases and plastic deformation affect the PCIs. (e) Illustration of how a thin film expands as a result of the absorption of hydrogen. For a thin film that is clamped to the substrate, the film can only expand in the out-of-plane direction $\varepsilon_{z,}$ and no in-plane expansion ($\varepsilon_{xy} = 0$) can occur. This results in the build-up of high in-plane stresses σ_{xy} in a thin film and the release of stress by strain in the out-of-plane-direction only. (f) Relationship between in-plane stress and the hydrogen-to-metal ratio x for elastic expansion, expansion that is elastic at low x and becomes plastic, and for a free standing film. (g–j) Different mechanisms in which the lattice in (g) can expand as a result of the absorption of hydrogen. The dots indicate lattice points. The figure is not to scale and a cubic lattice is selected for simplicity as the unexpanded lattice.

be described by Sievert's law. When the pressure is increased, more hydrogen will be absorbed. At higher pressures, elastic interactions between the hydrogen atoms start to dominate. At this point, the α-phase can no longer accommodate extra hydrogen and a high-hydrogen concentration β-phase starts to nucleate. As such, this phase transition is of first order. The fraction of the β-phase increases at the expense of the α-phase, and a plateau appears in the PCI. When the entire α-phase is transformed into the β-phase, a higher hydrogen pressure is again required to increase the hydrogen-to-metal ratio.

The hydrogen pressure at which the α-to-β phase transition occurs is commonly referred to as the plateau pressure. This transition is typically of first order, and an energy barrier needs to be overcome to nucleate the β-phase. As such, when the sample is unloaded, the pressure at which the β-phase transforms back to the α-phase is lower than for the reverse process. Therefore, the PCI curves are not the same for absorption and desorption of hydrogen and these appear as two distinct branches.

In general, the hydrogen-to-metal ratio and thus the PCI depends strongly on temperature. This can be described by Van 't Hoff's Law:

$$Ln\frac{P_{eq}}{P_0}=\frac{\Delta H}{RT}-\frac{\Delta S_0}{R}, \tag{3.2}$$

where T is the temperature, P_{eq} the equilibrium pressure (or plateau pressure), P_0 the standard pressure, R the universal gas constant, ΔH the enthalpy of hydrogenation [kJ/mol H_2], and ΔS_0 the entropy of hydrogenation [J/K/mol H_2]. The change in entropy is in first approximation determined by the loss in entropy when gaseous hydrogen is absorbed by the metal lattice (−131 J/K/mol H_2). However, in practice configurational and vibrational contributions have often a profound influence on the entropy: while the value for Mg is within 10% of −130 J/K (Cui et al., 2013; Zhou et al., 2014; Li et al., 2021), the deviation for Pd is substantially larger (−94 J/K/mol H_2) (Wicke & Nernst, 1964).

The enthalpy of hydrogenation corresponds to the amount of heat absorbed by the lattice when hydrogen is absorbed. It is typically quite negative for such elements such as Pd, Mg, Ta, V and Nb and heat is thus released when hydrogen is absorbed (Fukai, 2006). Since the enthalpy of hydrogenation is in most cases a negative number, the equilibrium pressure increases for certain hydrogen-to-metal ratios with temperature. Furthermore, if the temperature exceeds the critical temperature T_C, no phase transition is observed. Instead, a continuous increase of x with increasing pressure occurs within the solubility range of the hydride phase. As a result, the absorption and desorption branch of the PCI merge and no plateau pressure can be observed anymore. Instead, a gradual increase of x with increasing P_{H2} is observed.

3.2.2 Interface effects

The nature of a thin film makes the thermodynamics compared to bulk materials substantially different: as it is a relatively thin 2D structure, the surface-to-volume

ratio of a thin film is much larger than for a bulk material, leading to interface effects that can substantially affect the overall thermodynamics. Furthermore, a thin film is restricted in its volumetric expansion: owing to the 2D nature of the thin film and adhesive forces between the film and the substrate, the film can only expand in the out-of-plane direction as long as the adhesion with the substrate is intact. This effect is named clamping. As the expansion of the lattice is about 2–3 $Å^3$ per absorbed hydrogen atom (Fukai, 2006), the absorption of hydrogen can result in high in-plane stresses in the film that can significantly affect the thermodynamics. For instance, the expansion when MgH_2 is formed from Mg is about 30%. In sum, for thin films the bulk Gibbs free energy $\Delta G_{Bulk} = \Delta H_{Bulk} - T\Delta S_{Bulk}$ must be adjusted by:

$$Ln\frac{P_{eq}}{P_o} = \frac{\Delta G_{ThinFilm}}{RT} = \frac{\Delta G_{Bulk}}{RT} + \frac{\Delta G_{Interface}}{RT} + \frac{\Delta G_{Clamping}}{RT}. \tag{3.3}$$

Interface effects can significantly shift the position of PCIs. Taking the example of a two-phase system with a first-order phase transition (e.g., as in Pd and Mg), the PCIs exhibit a plateau pressure that is different for the absorption and dissociation isotherms. Interface effects can significantly shift the position of both isotherms, by the same amount. To understand how the isotherms can be shifted, let's consider $\Delta G_{interface}$, which is given by:

$$\Delta G_{interface} = \sum_i \left[\{A_i\gamma_i\}_{MH_x} - \{A_i\gamma_i\}_M \right] \tag{3.4}$$

where A_i is the interface area and γ_i the interface energy of interface i (Mooij et al., 2011). As such, one should correct the Gibbs free energy of the bulk metal hydride MH_x by the sum of the difference in interface energy of the metal hydride (MH_x) and metal (M) state, considering each interface i. This correction is thus proportional to the total interface energy area A. Assuming that the metal hydride thin film has the same interface on the top and bottom (e.g., sandwiched between two layers of the same material), one can deduce that the plateau pressure shifts by:

$$\mathrm{Ln}\frac{P_{ThinFilm}}{P_{Bulk}} = \frac{2V}{RTd}\Delta\gamma, \tag{3.5}$$

with V the molar volume of the host metal, T the temperature and d the thickness of the film (Mooij et al., 2011). $\Delta\gamma$ is the difference in interface energy, which can be both negative (shifting the plateau pressure downwards) or positive (shifting the plateau pressure upwards with respect to the bulk). As illustrated in Fig. 3.1c, this shift affects both the absorption and desorption branch of the PCI equally, and therefore does not result in a widening of the hysteresis gap. The assessment of Eq. (3.5) is intuitive: the thinner the layer, the larger the contribution of interface effects will be (an example will be presented in Section 11.4.1).

In general, the interface energy difference $\Delta\gamma$ strongly depends on the material surrounding the metal hydride as well as the crystallographic orientation of the interface. As thin films are often highly textured, the interface is predominantly aligned across one crystallographic facet of the material. Correspondingly, changing the orientation of the texture can affect the interface energy substantially.

3.2.3 Clamping, volumetric expansion and stress release

The 2D nature of a thin film ensures that a thin film metal hydride can only expand in the out-of-plane direction. As illustrated in Fig. 3.1e, this consequently results in high compressive in-plane stresses when the film is clamped to the substrate. When this stress increases is proportional to the hydrogen-to-metal ratio, we consider the linear-elastic regime. In this regime, the expansion of the material also scales with the hydrogen-to-metal ratio. When deviations from this regime occur, plastic deformations set in. We note that in a completely free-standing material, no in-plane build-up of stress occurs when the material absorbs hydrogen: stress can in this case be released freely in all directions. Compressive strain and plastic deformation have a different effect on the PCI: Whereas compressive strain results in an equal shift of the absorption and the desorption isotherms (Fig. 3.1c), plastic deformation widens the gap between the absorption and desorption isotherms (Fig. 3.1d).

To accommodate the volumetric expansion of hydrogen in a thin film, generally speaking there are three different mechanisms that we can discriminate if the substrate is rigid. In practice, a combination hereof can occur. Assuming no structural phase transition would occur in bulk, the first option is that the material expands isotropically, in a similar way as in bulk. As illustrated in in Fig. 3.1h, in such a case fewer unit cells can be accommodated in plane than in the unexpanded situation (Fig. 3.1g), and more unit cells need to be stacked on top. As such, this scenario requires large rearrangements of atoms. In the next scenario, the expansion is no longer isotropic, but completely in the out-of-plane direction. As illustrated in Fig. 3.1i this leads to a deformation on the unit cell that can either be plastic or elastic in nature. When stresses become too high and exceed the adhesion energy to the substrate, delamination of the film from the substrate can occur. This typically results in buckling, where the film is detached from the substrate at multiple locations. A significant body of literature has been devoted to measuring the in-plane stresses and adhesion energy, either by measuring the curvature of the substrate (Dornheim et al., 2003; Hamm et al., 2015; Laudahn et al., 1999; Nix, 1989; Pedersen et al., 2004) or by making use of X-ray diffraction measurements (Wagner et al., 2016).

Clamping can also affect the PCIs. To understand this, we consider the model by Schwarz and Khachaturyan (2006). According to this model, the incorporation of hydrogen in the host metal's lattice results in stresses, and thus strain. Consequently, this creates a thermodynamic barrier for a phase to be nucleated, and as such results in a difference between the absorption and desorption plateau pressures, creating an intrinsic hysteresis in the system. Here, intrinsic refers to the hysteresis present in a

material that is completely free to expand in all directions (e.g., not confined and clamped).[1] In a thin film, the situation is substantially different. As long as the film remains attached to the substrate, the system is constrained in expansion. In bulk, mechanical work can be minimised by rearrangements of the lattice upon hydrogen absorption. In thin films, additional mechanical work needs to be performed owing to these constraints on the expansion. If this expansion is elastic in nature, it shifts the PTIs to higher hydrogen pressures, and does so equally for the absorption and desorption branch (Fig. 3.1c). In case the effect is plastic, involving e.g., deformations of the unit cell, dislocations, and migration of atoms, the hysteresis gap widens (Fig. 3.1d).

Palladium is an example where clamping plays a profound role. Palladium has a phase diagram similar to the one illustrated in Fig. 3.1a, where the α-PdH_x and β-PdH_x phases are both face-centred cubic phases with different amounts of hydrogen absorbed, e.g., $x < 0.05$ for α-PdH_x and $x > 0.5$ for β-PdH_x at room temperature, depending on the thickness (Flanagan & Oates, 1991; Lewis, 1982; Manchester et al., 1994). To accommodate this expansion, in bulk the fcc structure will expand equally in all three directions (isotropic expansion). For thin films, this is not necessary the case. When adhesion conditions are good and films are thin, palladium remains clamped to the substrate and expands anisotropically (Harumoto et al., 2017; Laudahn et al., 1999; Pivak et al., 2011; Wagner et al., 2016; Wagner & Pundt, 2016). This is for example the case when an additional Ti adhesion layer is used between the substrate and a polycrystalline epitextured 40 nm Pd film on sapphire. In this case, a much larger out-of-plane expansion is observed (4.8%) than in bulk (3.6%) for $PdH_{0.6}$ w.r.t Pd. Because of that, the Pd unit cells deform, and in this case part of this deformation is plastic. This affects the PCI considerably: the hysteresis gap widens substantially (Pivak et al., 2011). Differently, when no Ti adhesion layer is used, the film buckles and the out-of-plane expansion becomes comparable to bulk. In such a case, stress can be released without plastic deformation and the hysteresis is similar to bulk (Pivak et al., 2011).

3.2.4 Critical temperature, enhanced solubility and suppression of phase transitions

Besides deformations of the unit cell, enlarged hysteresis, and shifting of PCIs, clamping and interface effects may change the metal-hydrogen phase diagram altogether: These effects can extend the solid-solution limit of hydrogen in the α-phase, or reshape the phase diagram by lowering the critical temperature. In some cases phase transitions may be suppressed completely as the hydride phase is destabilised. Clamping and the resulting compressive strain and/or deformation of the unit cell may also result in a reduction of the elastic hydrogen-hydrogen interaction that is responsible for the stability of the hydride phase (Feenstra et al., 1983; Salomons et al., 1987; Wagner & Horner, 1974; Wagner et al., 2016; Wagner & Pundt, 2016; Zabel & Peisl,

[1] We note that strictly speaking this model is only valid for completely coherent transitions, and even in bulk materials this is often not the case.

1979, 1980). In fact: in clamped systems the hydrogen-hydrogen interaction, attractive in free standing systems, may even become repulsive. In the case of palladium, clamping results in a modest suppression of the critical temperature and an increase in the solubility limit (Feenstra et al., 1983; Nicolas et al., 1986). These effects also occur when palladium is alloyed with gold, a common strategy to suppress the phase transition. In this case, a smaller gold concentration is in thin films needed to suppress the α-to-β phase transition than in bulk and a much large solubility in the α-phase is obtained than in either bulk or disk-shaped nanoparticles. However, hysteresis does not disappear completely even though the α-to-β is suppressed: residual hysteresis owing to the plastic deformation of the film is still present (Bannenberg, Nugroho, et al., 2019). Not all effects originate from clamping: size-dependencies are also seen for instance in palladium nanoparticles that have much more freedom to expand laterally (see, e.g., Baldi et al., 2014; Griessen et al., 2016; Syrenova et al., 2015).

Niobium thin films are another example where a profound impact of nanoconfinement on the phase diagram is observed (Burlaka et al., 2016; Dyck et al., 2024; Moehlecke et al., 1985; Ng et al., 1997; Song et al., 1997; Wagner et al., 2019; Wagner & Pundt, 2016; Zabel & Peisl, 1980). Indeed, depending on thickness, the solubility limits in the solid-solution α-phase increases, and the critical temperature in the phase diagram is reduced significantly. Wagner et al. (2019) report for epitaxial Nb films on sapphire a reduction in T_c from 170 °C (Fukai, 2006; Schober, 1996) to $T_c = 91$ °C for 40 nm, and to $T_c = -6$ °C for 5 nm thin films, i.e., below room temperature. Concomitantly, the hydrogen-to-metal ratio in which phase coexistence occurs is at room temperature reduced from $0.06 \leq x \leq 0.7$ to $0.12 \leq x \leq 0.5$ for 40 nm while phase transitions are completely absent for 5 nm thin films. Furthermore, they report that deformation is elastic and extends up to $x \approx 1$ for the thinnest films studied, while plastic deformations occur after a critical hydrogen-to-metal ratio. At this point, in-plane stresses are observed up to 10 GPa (Hamm et al., 2015).

In vanadium thin films, a similar effect was observed, and the critical temperature decreases substantially with decreasing thickness. This affects the phase-behaviour dramatically: The high-concentration ε-VH phase disappears at a temperature of 97 °C if the thickness of the vanadium film is reduced to 10 nm, while the low-concentration β-V_2H phase is suppressed if the thickness is further reduced to 5 nm (Bloch et al., 2010). Clamping does not necessarily need to originate from the interaction with the substrate: it can also originate from elastic constraints at interfaces with other layers, such as capping layers. Together with other finite-size effects, this has been studied extensively, as for example in vanadium superlattices, i.e., layers of vanadium alternated with another material (Andersson et al., 1997; Hjörvarsson et al., 1991; Xin et al., 2014; Xin et al., 2016). Nb/W superlattices (Olsson, 2002) or capped magnesium films (Baldi et al., 2009, 2018). In these case, interfacial control allows one to adjust the plateau pressures, solubility limits and/or critical temperature.

Tantalum is another material where nanoconfinement ensures a completely different tantalum-hydrogen phase diagram for thin film materials than for bulk (Bannenberg, Blom, et al., 2023). For a 40 nm Ta (110) thin film, deposited with a 4 nm Ti adhesion layer on quartz and capped with a 10 nm $Pd_{0.6}Au_{0.4}$ layer, the critical temperature can be suppressed from $T_c = 61$ °C to below −60 °C. Correspondingly, a

large solubility in the Ta α-phase is observed up to at least $TaH_{0.7}$. To accommodate the about 7% increase in volume, the tantalum unit cell deforms. Indeed, the 7% increase is completely translated into the out-of-plane (110) direction, while no expansion is observed in-plane. Despite this large deformation of the cubic unit cell, no hysteresis between loading and unloading is observed, and the expansion is completely proportional to hydrogen-to-metal ratio, indicating that the deformation is completely elastic in nature. The fact that nanoconfinement allows such a large solubility range within one phase, that the phase transitions are suppressed effectively, and that the deformation is complexly elastic in nature, makes tantalum an ideal material for hydrogen sensing (See Section 3.4.3).

3.3 Experimental methods

3.3.1 Thin film synthesis and deposition methods

One of the most widely applied techniques to synthesise metal hydride thin films is through magnetron sputtering (physical vapour deposition). As illustrated in Fig. 3.2, in magnetron sputtering a sample is positioned in a large vacuum chamber. In this deposition chamber disks of the target materials are also located. The substrates to be sputtered are typically positioned above these disks. Subsequently, a plasma is

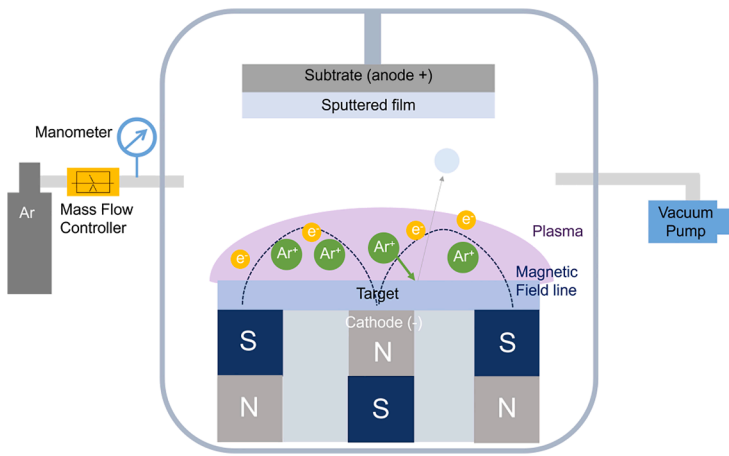


Figure 3.2 Schematic representation of a magnetron sputtering (physical vapour deposition) set-up. A magnetron set-up consists of a high vacuum chamber in which one or more disks of the material to be sputtered ('targets') are present. This target is placed opposite of the material to be sputtered (e.g., a substrate). During deposition, a plasma is created in the deposition chamber by applying a high voltage between the target and the substrate. This causes electrons to be accelerated and argon ions to be formed. These argon ions are directed to the target with the help of magnetic fields, knocking off atoms from the target. Part of these atoms end up on the substrate and a film can be grown.

created inside the deposition chamber by introducing a low pressure of an inert gas such as Ar and applying a high voltage between the cathode (located behind the target) and the anode (the substrate/ground/chamber). This causes electrons to be present in the sputtering gas to be accelerated away from the target and induce collisions with the gas molecules, ionizing the gas. To further enhance the density of ions, magnets ensure that the electrons are confined to the space just above the target. As a result, the target is continuously bombarded with high-energy ions causing atoms to be liberated from the target and to be (in part) deposited on the substrate.

The sputtering process can be controlled by the deposition pressure, the applied power during deposition, the temperature of the substrate and the sputter time. Alloys can also be created by simultaneously using multiple sputter targets at well-defined power ratios. To allow high-quality reproducible samples, one has to calibrate the relation between deposition rate (nm/second) and the sputtering power. To this end, 'tooling' samples can be made that are sputtered for a well-defined time and of which the thickness is accurately determined using reflectometry, ellipsometry, or a profilometer.

Other techniques frequently used to produce thin film metal hydrides include pulsed laser deposition, electron beam evaporation, thermal evaporation, all other examples of physical vapour techniques. In pulsed laser deposition, a pulsed laser is focused on a target material located in a vacuum chamber. Subsequently, a vapour of atoms is created that can be deposited on a substrate. Similarly, in electron beam deposition an electron beam is accelerated and steered to a target material present in a vacuum chamber. There, again, atoms are liberated and using these atoms a layer can be grown on a substrate. In thermal evaporation, a target material is heated to high temperatures, causing solid evaporation and the creation of a high vapour pressure. In this way the substrate is thus coated by the evaporation of atoms.

3.3.2 Hydrogenography (optical transmission measurements)

Optical transmission measurements of thin metal hydride films, also named hydrogenography, have been widely employed to study the pressure-composition/transmission-isotherms (PCI/PTI), determine the enthalpy/entropy of hydrogenation and study the hydrogenation kinetics. This technique takes advantage of the fact that when a metal hydride absorbs hydrogen, the optical transmission changes. This technique can both be used to study samples with very apparent changes in transmission, such as in magnesium where a metal-to-insulator transition occurs upon hydrogenation and the transmission increases by a factor ~10, or metal-hydride samples in which the optical transmission changes are much smaller, such as transition metals. This works provided that the transmission is at least about 1%, i.e., when the films are thin enough (typically $<$100 nm) (Gremaud et al., 2007).

Fig. 3.3a shows an overview of a typical hydrogenography set-up. The heart of the setup is a pressure cell in which one or more (gradient) thin film samples can be positioned. This pressure cell has optical windows, both on top and on the bottom, to allow diffuse light, originating from the light source below the cell, to transmit through the samples and the cell and subsequently be detected by a CCD/CMOS camera above the

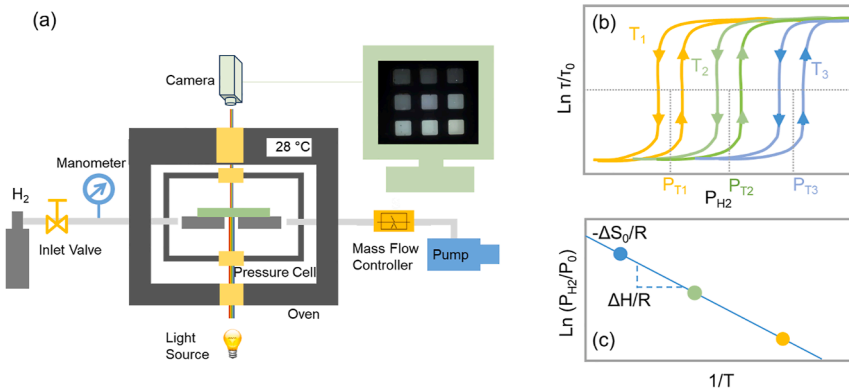


Figure 3.3 Principle of hydrogenography/optical transmission measurements. In a hydrogenography measurement (panel a), different samples (in the example nine samples) are placed inside a temperature-, pressure- and flow-controlled cell. This cell has optical windows at the top of the bottom. Light, coming from below, illuminates the samples and a camera records the optical transmission of the sample in transmission. The optical transmission is then averaged over the sample and can be plotted for each temperature as a function of the partial hydrogen pressure, yielding Pressure-Transmission-Isotherms (panel b). The transmission τ is often normalised to the initial transmission τ_0 and the natural logarithm is taken of this ratio. Typically, measurements are performed by both increasing and decreasing pressure and for multiple temperatures. By making the assumption that each value of $Ln(\tau/\tau_0)$ corresponds to a specific hydrogen-to-metal ratio of the sample, one can use this to construct Van 't Hoff plots and determine the enthalpy ΔH and entropy ΔS_0 of hydrogenation (panel c). In a Van 't Hoff plot, the natural logarithm of the equilibrium pressure normalised to the standard pressure P_0 is plotted for a given $Ln(\tau/\tau_0)$ as a function of the inverse temperature. By fitting a linear line through these points, the enthalpy and entropy can be deduced from the slope and intercept, respectively.

set-up (see camera image in Fig. 3.3a for an example). Inside the cell, the partial hydrogen pressure $P_{H2} = c_{H2}P_{tot}$ can be controlled, either by changing the total pressure P_{tot}, or by mixing e.g., H_2 with Ar in various ratios with mass flow controllers to change the hydrogen concentration of the gas flow c_{H2} while keeping the total pressure fixed. Furthermore, the pressure cell is typically placed inside an oven allowing control of the sample temperature.

Hydrogenography allows the quick screening of the thermodynamic properties of metal-hydride thin films. In a typical experiment, one exposes multiple samples to a stepwise increasing and decreasing partial hydrogen pressure and records the optical transmission of the samples. These optical transmissions are recorded with a CCD/CMOS camera and typically averaged over the sample area. Then, one obtains the pressure-transmission-isotherm (PTI) for each sample, i.e., the optical transmission is obtained as a function of the partial hydrogen pressure. This is analogue to the pressure-composition-isotherms (PCI). These PTIs are typically recorded at multiple temperatures and allow one to determine important parameters such as plateau pressure, hysteresis (gap), and the enthalpy/entropy of hydrogenation. Indeed, assuming

that each transmission corresponds to a specific hydrogen-to-metal ratio allows one to determine how the pressure at which this transmission is achieved variates with temperature. Then, one can use these pressures (as e.g., the plateau pressure) to compute the enthalpy and entropy with Van 't Hoff's relation (Eq. 3.2): when making a plot of $Ln\ (P/P_0)$ vs $1/T$ the intercept corresponds to $\Delta S_o/R$ and the slope to $\Delta H/R$.

To directly relate the PTIs to the PCIs one needs information on the relation between the optical transmission dependence on the hydrogen-to-metal ratio in the sample. Ignoring e.g., reflections, at first approximation the optical transmission of a thin film is given by Beer–Lambert's law:

$$Ln\ \tau(P_{H2}) = \alpha(P_{H2})d \tag{3.6}$$

where $\tau(P_{H2})$ is the optical transmission at a certain partial hydrogen pressure, α the linear attenuation coefficient and d the thickness of the film. Then, we can deduce that the change in transmission of the thin film with respect to the transmission of the unloaded state τ_{unl} is given by:

$$Ln\frac{\tau(P_{H2})}{\tau_{unl}} = (\alpha(P_{H2}) - \alpha_{unl})d \tag{3.7}$$

For a two-phase system with varying phase fractions, it turns out that $Ln\frac{\tau(P_{H2})}{\tau_{unl}}$ is proportional to the hydrogen-to-metal ratio. For a varying hydrogen-to-metal ratio within one phase (e.g., solid solution of the host-metal and hydrogen) this is not necessarily the case. However, it turns out that often such a result is observed for the white light optical transmission. Indeed, for e.g., palladium-gold, tantalum, hafnium, tantalum-ruthenium and vanadium alloys such a linear relation between the hydrogen-to-metal ratio and $Ln\frac{\tau(P_{H2})}{\tau_{unl}}$ has been identified (Boelsma et al., 2017; Bannenberg, 2023; Tsakiris et al., 2024; Nugroho, Darmadi, et al., 2018; Bannenberg, Boelsma, et al., 2019; Nugroho et al., 2019; Palm et al., 2019; Prinz et al., 2010). Nevertheless, there are exceptions where such a relation does not hold, as e.g., $V_{80}Zr_{20}$ metallic glass (Bylin et al., 2024), or for tantalum it has been identified that it does not hold for all wavelengths (Palm et al., 2018; Bannenberg, Verhoeff, et al., 2024). As such, one should e.g., use neutron reflectometry or quartz-crystal microbalance measurements to verify whether such a relationship is applicable.

Besides studying the equilibrium thermodynamics, hydrogenography can also be used to study the kinetics of hydrogenation. Roughly speaking, two methods exist: one to study the diffusion in the in-plane direction, and one to study the kinetics of hydrogen transport in the out-of-plane direction. The kinetics in the in-plane direction have been studied by preparing a special sample (see Fig. 3.4c) (Bannenberg, Boelsma, et al., 2019; de Man et al., 2013; Westerwaal et al., 2015). In this sample, the material of interest, in the example tantalum, is sandwiched between two Ti layers to prevent mixing and promote adhesion. Subsequently, an yttrium indicator layer is deposited on top. At last, well-separated dots of palladium are deposited on top of the yttrium.

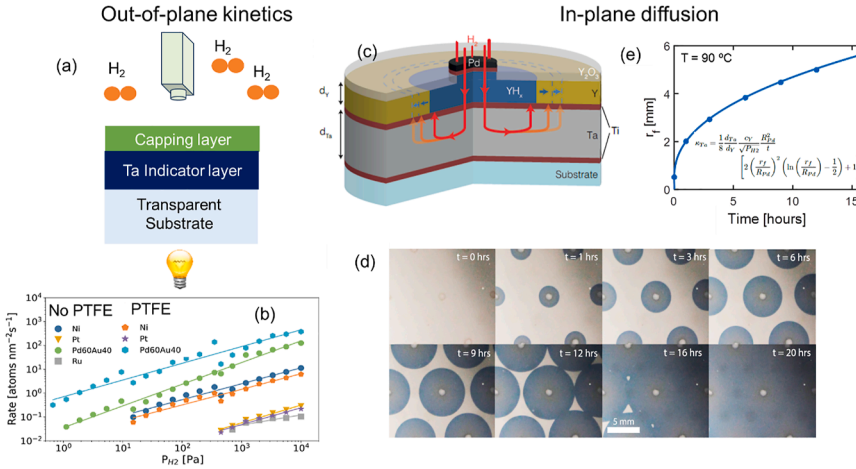


Figure 3.4 Different ways to study the hydrogenation kinetics/diffusion of materials by optical transmission measurements. There are different ways to study the hydrogenation kinetics/diffusion of materials by optical transmission measurements. One can study the diffusion/dissociation kinetics of e.g., a (capping) layer by using a Ta indicator layer. When hydrogen is dissociated by and diffuses through the capping layer, it is absorbed by the Ta indicator layer, causing an optical change. This change in optical transmission can be detected, and if the relation is known between the (changes in the) optical transmission and the hydrogen-to-metal ratio, one can determine the absolute hydrogenation rate. (b) Example of the hydrogenation rate of different capping layers studied using the sample of (a). The capping layers indicated have been studied both with and without an additional PTFE coating, which accelerates the response of the $Pd_{0.6}Au_{0.4}$ layer. Diffusion can also be studied in-plane using the sample demonstrated in (c). Here, the material trough which diffusion is studied is deposited on a substrate. On top of it, an yttrium indicator layer is deposited, which partly oxidises from the top. On top of the Y layer, Pd dots with a diameter of 0.9 mm are deposited that are organised in a hexagonal manner. Hydrogen can only be supplied through the Pd dots, has to diffuse through the YH_x and in-plane through the Ta layer as the in-plane diffusion through YH_x is slow. The absorption of hydrogen by YH_x causes a metal-to-insulator change, which is clearly visible in (d) by taking images in transmission. By determining the position of the diffusion front radius r_f as a function of time, one can determine the hydrogen permeation. The continuous line indicates a fit of the equation to the data.
Figures (a–b) adapted from Bannenberg, L. J., Boshuizen, B., Ardy Nugroho, F. A., & Schreuders, H. (2021). Hydrogenation kinetics of metal hydride catalytic layers. *ACS Applied Materials and Interfaces, 13*(44), 52530–52541. https://doi.org/10.1021/acsami.1c13240; (c) from Westerwaal, R. J., et al. (2015). The hydrogen permeability of Pd–Cu based thin film membranes in relation to their structure: A combinatorial approach. *International Journal of Hydrogen Energy, 40*(10), 3932–3943, https://doi.org/10.1016/j.ijhydene.2015.01.124. Figures (d–e) from Bannenberg, L. J., et al. (2019). Optical hydrogen sensing beyond palladium: Hafnium and tantalum as effective sensing materials. *Sensors and Actuators B: Chemical. 283*, 538–548, https://doi.org/10.1016/j.snb.2018.12.029 with permissions.

The working principle relies on the yttrium indicator layer, which changes colour when absorbing hydrogen and forming yttrium hydride. When the sample is exposed to hydrogen, the hydrogen can only enter the sample through the palladium dots that act as a source of atomic hydrogen. Indeed, only at this location molecular hydrogen is dissociated into atomic hydrogen. Subsequently, yttrium hydride is immediately formed underneath the Pd dots. As the diffusion of hydrogen through yttrium hydride is extremely slow ($D \approx 10^{-11}$ cm/second) (Di Vece & Kelly, 2003), and in this case much slower than to the material of interest (tantalum), lateral transport of hydrogen occurs only through the tantalum layer. This hydrogen will be immediately absorbed by the yttrium layer, forming yttrium hydride and changing colour. As such, one can study the diffusion of hydrogen through the tantalum layer by tracking the growth of the yttrium hydride islands that are easily visible (Fig. 3.4c). Fitting the diffusion rate, one can then determine the hydrogen permeation constant (Fig. 3.4d).

The hydrogenation kinetics in the out-of-plane can also be studied. This methodology has for example been applied to study the hydrogenation kinetics of catalyst layers that can be used in e.g., hydrogen sensors. In such a layer, molecular hydrogen, present in the environment, is dissociated into atomic hydrogen that can be absorbed and diffuse through the material. To study which material provides the highest catalytic activity, determine the activation energy and the rate of hydrogenation, various materials (with and without a PTFE coating that can potentially reduce the activation energy) where deposited on a 40 nm Ta indicator layer (Fig. 3.4a and b). Subsequently, the hydrogenation kinetics were monitored for several partial hydrogen pressures and temperatures. Based on this, and as $\Delta Ln\frac{\tau(P_{H2})}{\tau_{unl}}$ for tantalum is proportional to the hydrogen-to-metal ratio, the hydrogenation rate R can be approximated:

$$R = 0.9c\frac{d\rho\Delta Ln\dfrac{\tau(\mathrm{P_{H2}})}{\tau_{unl}}}{t_{90}M}, \tag{3.8}$$

where d is the thickness of the Ta indicator layer, ρ the density, M the molar mass, c a constant relating the $\Delta Ln\frac{\tau(P_{H2})}{\tau_{unl}}$ to the change in the hydrogen-to-metal ratio (e.g., obtained from neutron reflectometry) and t_{90} the time it takes to achieve 90% of the response. Subsequently, the partial hydrogen pressure dependence of the hydrogenation rate allows one to say if the kinetics are diffusion limited ($R \sim \sqrt{P_{H2}}$) or limited by interface processes such as the hydrogen dissociation process ($R \sim P_{H2}$) (Borgschulte et al., 2006). When considering the temperature dependence of the hydrogen, one can, using Arrhenius law, determine the apparent activation energy. In this case, it was found that palladium-gold layers provide significantly higher hydrogenation rates than pure palladium (Bannenberg, Boshuizen, et al., 2021), and that the coating with PTFE can lower the activation energy by a factor of two owing to the formation of bonds between Pd and the PTFE layer (Bannenberg, Boshuizen, et al., 2021; Nugroho et al., 2019). Another application of studying the

kinetics in the out-of-plane direction is to study the barrier function of layers, which has e.g., been performed for Ru in combination with an yttrium indicator layer (Soroka et al., 2020).

3.3.3 Neutron and X-ray reflectometry

Neutron and X-ray Reflectometry are non-destructive experimental techniques that can be used to study the thickness, composition and roughness of thin films and other flat surfaces that are composed of layers with thicknesses of about 1–300 nm (see, e.g. (Fritzsche & Huot, 2016), or (Dura et al., 2017). In the context of thin film metal hydrides, X-ray reflectometry has mainly been used to study the thickness of layers, while neutron reflectometry has been used to study the hydrogen-to-metal ratio of the thin film. Both techniques allow for in-situ studies, e.g., under different (partial hydrogen) pressures and for different temperatures.

As illustrated in Fig. 3.5a, reflectometry relies on illuminating a sample by either neutrons or X-rays under a small incident angle. These neutrons or X-rays are then

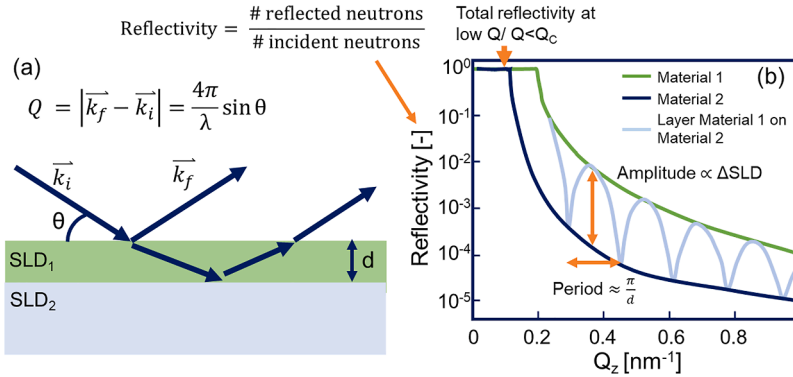


Figure 3.5 Principle of reflectometry. (a) Schematic representation of a reflectometry experiment. In a neutron or X-ray reflectometry experiment, a beam of neutrons or X-rays illuminates a sample under a small angle of incidence θ. This beam is partly reflected by the sample and detected by the detector. The fraction of neutrons or X-rays reflected is named the reflectivity. An example neutron reflectogram is provided by panel (b), which displays the reflectivity as a function of Q. Q is the momentum transfer of the neutron/X-ray when reflected by the sample and combines the effect of the wavelength and incident angle on the reflectivity in a single parameter. For a material with a different index of refraction/scattering length density (SLD), the reflectogram changes. Note that the angles in the schematic are largely exaggerated and the reflectivity is plotted on a logarithmic scale. Each material, as a substrate, has a different reflectogram and critical edge, i.e., the maximum Q at which the reflectivity is 1. When a layer of a material is deposited on a substrate of another material, interference occurs between neutrons/X-rays that are reflected from the surface of the sample and those that are reflected from the interface between the material. This interference gives rise to so-called 'fringes' in the reflectogram, of which the width is related to the thickness of the material and the amplitude to the difference in SLD.

partially reflected by the thin film and detected by a detector. In this way, the relative number of neutrons or X-rays reflected, i.e., the reflectivity of the sample, is determined:

$$Reflectivity = \frac{number\ of\ neutrons\ or\ X-rays\ reflected}{number\ of\ neutrons\ or\ X-rays\ incident}. \tag{3.9}$$

As the reflectivity depends both on the incoming angle θ (sometimes named glancing angle) and λ, the wavelength of the neutron or X-ray, the reflectivity is typically plotted as a function of the momentum transfer of the neutron or X-ray upon reflection Q. Q incorporates both the effect of the wavelength and the glancing angle:

$$Q = \frac{4\pi}{\lambda} \sin\theta, \tag{3.10}$$

As such Q can be varied by changing the incoming angle and keeping the wavelength the same, which is done in X-ray reflectometry. In neutron reflectometry, one can also keep the incident angle the same and vary Q by changing the wavelength (in fact measuring multiple wavelengths simultaneously).

3.3.3.1 Reflectivity of a slab of material

An example of typical reflectometry data is shown in Fig. 3.5b. The data, typical of a slab of material, as e.g., a substrate, shows how the reflectivity changes as a function of Q. Ignoring absorption (which can play a role for X-rays), for small values of Q, all neutrons/X-rays are reflected, and thus total reflection occurs. After a critical value of Q, Q_c, the reflectivity drops and becomes proportional to Q^{-4} (note the logarithmic scale). The value of Q_c is different for every material and depends on the index of refraction, or as we will see later, the scattering length density (SLD).

When we consider the simplest layered structure, a thin layer with thickness d on top of a substrate, the neutrons and X-rays can either reflect of the top surface, or the interface between the layer and the substrate. As illustrated in Fig. 3.5b and similar to the case of optical light reflecting from a surface (i.e., Fresnel optics), the interference between the radiation reflected of the top surface and the substrate-layer interface results into a reflectogram that is no longer smooth but contains fringes. The periodicity of these fringes ΔQ depends on the thickness of the layer and is in good approximation provided by:

$$\Delta Q \approx \frac{2\pi}{d}. \tag{3.11}$$

Differently, the amplitude of the fringes is predominantly determined by the contrast in SLD and provides information on the composition of the thin film.

3.3.3.2 Contrast and scattering length density: The case of neutrons and X-rays

While in optics typically the index of refraction is used to describe the reflection of light, in X-ray and neutron reflectometry it is more convenient to use a parameter called the scattering length density (SLD). This is a parameter that combines the number of atoms of material i per unit of volume, i.e., the atomic number density of atom/isotope i, N_i, with a measure on how strong each of these atoms/isotopes scatter. As neutrons mainly interact with the nucleus of an atom, and X-rays interact with the electrons around the nucleus, the *SLD*s are different for neutrons and X-rays, but the formalism is the same. For neutrons, the *SLD* is given by:

$$SLD = \sum_{i=1}^{n} N_i b_i(neutrons), \tag{3.12}$$

where b is the (coherent) neutron scattering length. This is an isotope-dependent quantity that can be found in tables (e.g., Sears, 1992). For X-rays, the *SLD* is given by:

$$SLD = \sum_{i=1}^{n} N_i f_i(0)(\mathrm{X-rays}). \tag{3.13}$$

Thus, the *SLD* is different for X-rays and neutrons. For X-rays, the *SLD* is the product of the atomic number density and the atomic form factor at $Q = 0$, $f(0)$, and then the sum over all elements n in the sample. $f(0)$ can be approximated by:

$$f_0 = f_1 + if_2 \approx r_e Z + i\frac{\sigma_a}{2\lambda}, \tag{3.14}$$

where r_e is the classical electron radius, Z the number of electrons of the element. For the imaginary component, which describes the absorption of X-rays, it is determined by σ_a, the absorption cross-section, and the wavelength of the X-ray, λ. As such, the imaginary component of the scattering length (density) describes the absorption. For neutrons, absorption, and as such the imaginary component of the *SLD*, can for almost all elements be ignored.

The fact that the *SLD* is different for X-rays and neutrons allows one to probe different properties with both types of radiation. To first approximation, the X-ray *SLD* is proportional to the electron density. As such, the higher the electron density, the higher Q_c will become.

For neutrons, the situation is more complex in that sense: the scattering length b shows no clear correlation with the atomic number. This is actually an advantage, as e.g., the incorporation of hydrogen (one of the few isotopes with a negative b, $b = -3.7$ fm) has a large influence on the *SLD* when it is incorporated in a metal as e.g., Pd has a strong positive scattering length, $b = 5.91$ fm.

3.3.3.3 *Example: Determining the hydrogen-to-metal ratio of tantalum thin films*

To illustrate the power of reflectometry, we consider the study of the difference in the partial hydrogen dependence of the hydrogen-to-metal ratio and layer thickness expansion of body-centred cubic α-Ta and tetragonal β-Ta (Fig. 3.6a). These films can be grown by carefully selecting the material on which they are grown: if grown directly on fused quartz, β-Ta tends to be crystallised, whereas α-Ta can be grown if a 4 nm Ti seed layer is used (Bannenberg, Verhoeff, et al., 2024). As such, for this study two samples were prepared: one with (i) a 4 nm Ti adhesion/seed layer, a 40 nm α-TaH_x layer, and a 10 nm $Pd_{0.4}Au_{0.6}$ capping layer, and a thin film composed of (ii) a 40 nm β-TaH_x layer, and a 10 nm $Pd_{0.4}Au_{0.6}$ capping layer

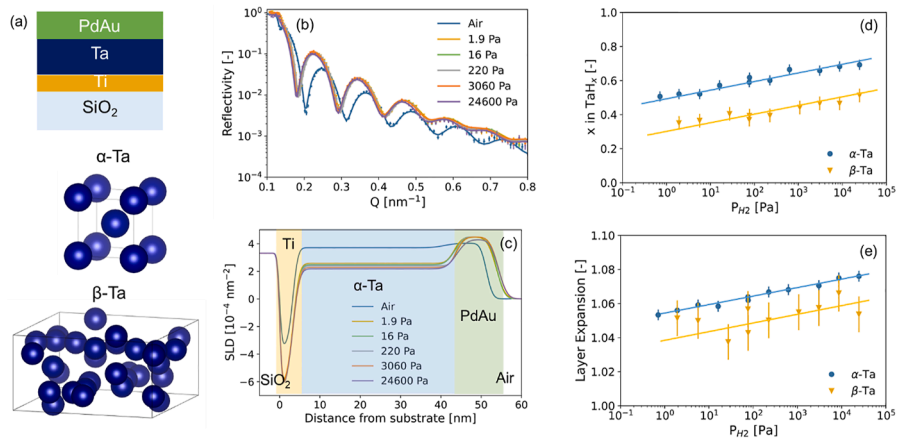


Figure 3.6 Example of neutron reflectometry data. Neutron reflectometry results to determine the hydrogen-to-metal ration and layer expansion of a 10 nm (nominal) $Pd_{0.6}Au_{0.4}$ capped 40 nm Ta film with either the α-Ta bcc structure or a β -Ta tetragonal structure. The α-Ta film has a 4 nm Ti adhesion layer and is deposited on a fused quartz substrate. (a) Schematic of the sample and visualisations of the crystal structures made with Vesta. (b) Neutron reflectometry results of the film exposed at room temperature to the different partial hydrogen pressures indicated. In the figure, the points represent the data measured, whereas the continuous line represent a fit to a 3-layer model. Based on this fit, i.e., the fitted thickness, SLD and roughness for each layer of the sample, the SLD profile of (c) can be constructed and the hydrogen-to-metal ratio and expansion calculated. (d) Partial hydrogen pressure dependence of the hydrogen-to-metal ratio. (e) Partial hydrogen pressure dependence of the layer expansion.

Figures (b + c) adapted from Bannenberg, L.J., Blom, L., Sakaki, K., Asano, K., & Schreuders, H. (2023). Completely elastic deformation of hydrogenated Ta thin films. *ACS Materials Letters*, *5*(4), 962-969. 10.1021/acsmaterialslett.3c00038. Available from: https://pubs.acs.org/page/amlcef/about.html, Figures (d + e) from L.J. Bannenberg, et al. (2024). Structural and optical properties of thin film β-Ta upon exposure to hydrogen to asses its applicability as hydrogen sensing material. American Chemical Society, *ACS Applied Nano Materials, 7*(2), 1757–1766. doi: 10.1021/acsanm.3c04902.

were synthesised. Both films were deposited on fused quartz substrates that are polished flat and have a low roughness (<0.5 nm). For X-ray reflectometry, 10×10 mm^2 substrates were used, while for neutron reflectometry larger 3-inch disk-shaped substrates were used to maximise intensity. During both the X-ray and neutron reflectometry experiments, the samples were exposed to different partial hydrogen pressures at a constant temperature. Details on the cell used for the neutron reflectometry measurements can be found in Bannenberg, Van Exter et al. (2024).

Fig. 3.6b shows the neutron reflectometry data acquired at different partial hydrogen pressures for α-Ta at the Delft Neutron Reflectometer (Bannenberg, Bresser, et al., 2023). With increasing partial hydrogen pressure, we see a change of the period of the fringes: the period is reduced, reflecting according to Eq. (3.11) an increase in the layer thickness. This can also be seen in the corresponding X-ray reflectometry data (Figure S10 of Bannenberg, Blom, et al., 2023). Furthermore, we see a change in amplitude: This is due to the fact that both the Ti layer ($b = -3.7$ fm) and the Ta layer ($b = 6.9$ fm) absorb hydrogen, causing a decrease of the SLD as the scattering length of H is negative ($b = -3.7$ fm). The incorporation of hydrogen also has a profound influence on the reflectivity around the critical edge, i.e., around Q_c. We emphasise that these changes cannot be discerned from the X-ray data. As the electron density of the material only marginally changes with the absorption of hydrogen, and X-rays are only sensitive to the electrons surrounding the nucleus, X-ray reflectometry does not allow for a direct quantification of the hydrogen-to-metal ratio and only sees the expansion as a result of the absorption of hydrogen.

To obtain detailed estimates of the SLD, thickness and the roughness, the data is fitted to a model. This can be done with programs like GenX (Björck & Andersson, 2007; Glavic & Björck, 2022) and Motofit (Nelson, 2006). In this case, a three (α-Ta) or two-layer (β-Ta) was used. Fitting it provides, besides estimates for the SLD, thickness and roughness of each layer, an SLD profile. Examples of SLD profiles, obtained by fitting the data of Fig. 3.6b, is provided in Fig. 3.6c. The SLD profile, which is a visual representation of the SLD as a function of the distance from the substrate, clearly shows all the different layers. In this profile, one can also discern that the Ta layers expands and that the SLD of the layer drops when exposed to a hydrogen pressure. This occurs owing to the incorporation of hydrogen in the layer.

From the fitted SLD and layer thickness, one can quantify the expansion as well as the hydrogen-to-metal ratio using:

$$x = \left(\frac{SLD_{MHx}}{SLD_M} \frac{d_{MHx}}{d_M} - 1 \right) \frac{b_M}{b_H}. \tag{3.15}$$

For a full derivation of this formula we kindly refer the reader to Bannenberg, Verhoeff, et al. (2024). The resulting partial hydrogen pressure dependence of the hydrogen-to-metal ratio (Fig. 3.6d) and expansion (Fig. 3.6e), indicate a pronounced

effect of the crystal structure. Indeed, at a given partial hydrogen pressure, β-Ta expands substantially less hydrogen than α-Ta, with a smaller expansion as a result. However, the increase in volume per hydrogen atom absorbed of the material is the same.

3.3.3.4 Alternative techniques to determine the metal-to-hydrogen ratio in thin films

Besides neutron reflectometry, other techniques have been used to determine the hydrogen-to-metal ratio in thin film metal hydrides. For example, nuclear reaction analysis (NRA) uses a monochromatic beam of ^{15}N ion that are accelerated to a specific energy (Fritzsche & Huot, 2016; Wilde & Fukutani, 2014). This ion beam reacts with the ^{1}H atoms present in the sample. In this reaction an excited ^{16}O nucleus is formed that subsequently relaxes to the ^{12}C ground state while emitting an α and γ(4.44 MeV) particle:

$$^{15}N + {}^{1}H \rightarrow {}^{16}O \rightarrow {}^{12}C + \alpha + \gamma(4.44\ \text{MeV}) \tag{3.16}$$

As such, one can indirectly measure the number of hydrogen atoms present in the sample by counting the number of emitted gammas with this specific energy. To obtain a depth-resolution one can scan the incident's beam energy. Typically, one can obtain a 1–5 nm depth resolution and detect relatively low (>100 ppm) hydrogen concentrations. Similar to reflectometry, NRA requires the samples to be flat in order to obtain a good depth resolution. However, NRA experiments are typically performed under vacuum or low pressures and can thus mainly be used to quantify the hydrogen-to-metal ratio in stable hydrides (such as YH_2).

Another technique that can be used is time-of-flight secondary ion mass spectroscopy (ToF-SIMS) (Paudel et al., 2024). In this technique, a focused ion beam illuminates the sample with the purpose to eject secondary ions from the sample. These secondary ions can then be detected using a time-of-flight mass analyser, which can determine the mass-to-charge ration of the secondary ions. In this way, an estimate of the metal-to-hydrogen ratio can be obtained.

Quartz-crystal microbalance (QCM) also allows the determination of the hydrogen-to-metal ratio. In this technique, a film can be deposited on a quartz crystal. The quartz crystal acts as a resonator with a specific resonating frequency (Bucur et al., 1976; El Far et al., 2012). When the QCM with the thin film on top is exposed to hydrogen, the mass of the material changes slightly, causing a shift of the resonance frequency. As such, one can quantify the amount of hydrogen absorbed by the material when exposed to different condition (gas pressure, temperature, etc.). Limitations of the technique include that it provides no depth resolutions and that it is not element specific: if the film e.g., oxidises a change in mass can also be detected. Moreover, for thin films the build-up of high in-plane stresses can also affect the resonance frequency. Therefore, this technique has found most usage in the quantification of the hydrogen-to-metal ratio by other nanostructures such as nanoparticles.

3.4 Applications and recent developments

3.4.1 Hydrogen storage

Metal hydrides have been extensively studied as hydrogen storage materials. This is particularly attractive as the volumetric hydrogen density in metal hydrides (e.g., 110 g/L for MgH_2) can be higher than liquid hydrogen (71 g/L) or compressed hydrogen (83 g/L at 1000 bar, RT). Among all the different candidates for hydrogen storage, such as TiFe, metalborohydrates, alienates, complex metal hydrides, magnesium is one of the main candidates. To illustrate the use of thin films for this application, we therefor focus on this material. Magnesium is particularly attractive because when it forms the metal hydride phase MgH_2 has a relatively high gravimetric and volumetric hydrogen density of about 7.6 wt/% H and of 110 g/L (Crivello et al., 2016; Song et al., 2023; Yartys et al., 2019). Furthermore, magnesium is a relatively cheap and abundant element: about 0.1 wt% and 3 wt% of the earth's sea and crust is composed of magnesium, respectively.

There are some key challenges for magnesium to solve before magnesium can be used as a solid-state hydrogen storage medium. This is in particular true for the sluggish kinetics and unfavourable thermodynamics resulting from the enthalpy of hydrogenation of $\Delta H = -74$ kJ mol_{H_2} and the entropy of hydrogenation of $\Delta S = 133$ J K mol_{H_2}. This dictates that while magnesium readily forms a hydride at relatively low hydrogen pressures at room temperature, high temperature (>250 °C) and/or low hydrogen pressures are required to dehydrogenate magnesium. In addition, as the dehydrogenation is an endothermic process, thermodynamics dictates that reasonable amount of heat needs to be supplied to desorb magnesium hydride. For hydrogen storage applications, an equilibrium pressure of 1–10 bar at temperatures between 25 and 150 °C are required, implying that the ΔH should become less negative. In addition, as the desorption of hydrogen is endothermic, implying that heat needs to be supplied to desorb the hydrogen from magnesium hydride. Furthermore, the relatively large volumetric expansion of 30% when magnesium hydride is formed makes it a challenge to achieve a high number of (un)loading cycles.

Magnesium hydride needs to be destabilised to become a suitable material for hydrogen storage. In other words, the enthalpy of hydrogenation should become less negative. To achieve this, nanostructuring and alloying have been two of the main techniques. In this quest, thin films are used as model systems as they allow a great control over composition and a means to alter both the interface (energy) and strain in a controlled manner. Furthermore, thin films have been studied extensively to understand the kinetics of hydrogenation (Hadjixenophontos et al., 2017; Mooij & Dam, 2013; Uchida et al., 2015; Vermeulen et al., 2009)

3.4.1.1 Size-effects

Studying how size effects can through elastic clamping and interface effects help to destabilise magnesium is an area of frequent study, albeit it is often difficult to discriminate between these two effects. Fig. 3.7 displays an example of a study on

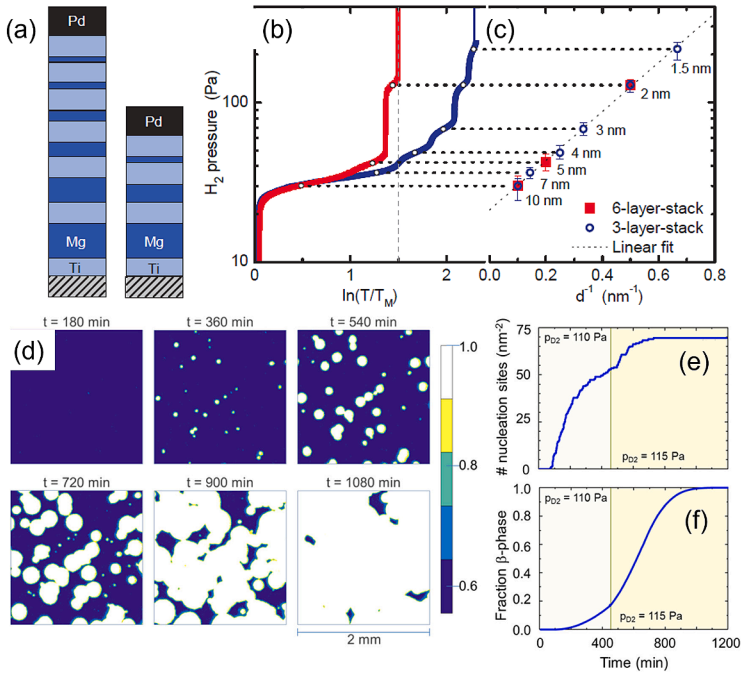


Figure 3.7 Thin film magnesium hydrogenation thermodynamics and kinetics studied with optical transmission measurements. (a–c) Example of the thickness dependence of the hydrogenation pressure in magnesium thin films. (a) Shows a multilayer stack with different thicknesses of magnesium layers sandwiched between Ti layers and capped with a Pd layer. (b) Shows the relative change in optical transmission relative to the transmission of the unloaded state (T_m) as a function of hydrogen pressure. (c) Layer thickness dependence of the plateau pressure of Mg thin films. (d–f) Study of the hydrogenation of a 10 nm Mg thin film sandwiched between two 10 nm Ti layers and capped by 10 nm Pd. (d) Top-view images of the sample in transmission at various moments in time during hydrogenation. The β-MgD_{2-y} domains transmit more light and are therefore brighter than α-MgD_x. Both nucleation and growth occur. (e) Number of nucleation sites as a function of time. (f) Fraction of β-MgD_{2-y} as a function of time. The increase in pressure resulted in an accelerated conversion of α-MgD_x to β-MgD_{2-y}, which is both due to an increased number of nuclei and an increase in radial growth velocity. Figures (a–c) adapted from Mooij, L. P. A. (2011), Interface energy controlled thermodynamics of nanoscale metal hydrides. *Advanced Energy Materials, 1*(5) (2011), 754–758, doi: 10.1002/aenm.201100316 and Figures (d–f) adapted from Bannenberg, L. J. et al. (2016). Impact of nanostructuring on the phase behavior of insertion materials: The hydrogenation kinetics of a magnesium thin film. American Chemical Society, *Journal of Physical Chemistry C, 120* (19), 10185–10191 with permission.

thickness effects. Here two different multilayer films with different thicknesses of magnesium layers sandwiched between Ti layers and capped with a Pd layer (Fig. 3.7a) are studied using optical transmission measurements (hydrogenography). In the optical transmission measurements, performed as a function of the

partial hydrogen pressures, distinct plateaus in the optical transmission are seen that correspond to the hydrogenation of the different magnesium layers. Indeed, the plateau pressure for both absorption and desorption of hydrogen increases substantially with decreasing thickness (Mooij et al., 2011). Based on this one can conclude that magnesium can be destabilised by reducing the thickness of the layer, or in bulk, by making tiny clusters of Mg in a matrix. Different from multilayer stacks, similar experiments have also been performed with samples that have a thickness gradient. Furthermore, it has also been shows that the thermodynamics of magnesium thin films can be tuned by elastic means, e.g., by sandwiching magnesium with different materials (Baldi et al., 2009, 2018).

3.4.1.2 Kinetics

Thin films have also been studied to determine the mechanisms and kinetics of hydrogenation of magnesium. One major reason why the hydrogen absorption kinetics in (bulk) magnesium is sluggish is the very small diffusivity in the β-MgH_2 that is orders of magnitude smaller than α-Mg. As such, when β-MgH_2 is formed, it 'blocks' the further hydrogenation of magnesium (see, e.g., Cho et al., 2023; Lin et al., 2022; Rydén et al., 1989; Uchida et al., 2015; Uchida et al., 2011; Zhdanov et al., 1993).

In thin films, there are several steps involved in the absorption of hydrogen. It involves the physisorption of H_2 on the surface, the dissociation of the H_2 molecule, the chemisorption and diffusion of H into magnesium, and the formation of MgH_2 (see, e.g., Cho et al., 2023). Mooij and Dam (2013) studied the hydrogenation of a 10 nm Mg thin film sandwiched between two 10 nm Ti layers that also avoid alloying with the 10 nm Pd. They show that hydrogenation can occur through a nucleation and growth mechanism. Here, magnesium hydride is nucleated at distinct nucleation sites. This can be observed in optical transmission measurement: α-Mg is a metal with a low optical transmission, while β-MgH_2 is an insulator with a high optical transmission, thus appearing bright in a top-view image of the thin film. As illustrated in Fig. 3.7d–f, once domains are nucleated subsequent growth occurs radially outward with the β-MgH_2 phase expanding at the expense of the α-Mg phase, following a nucleation-and-growth mechanism. While in bulk the α-Mg phase has a very small hydrogen solubility, neutron reflectometry indicates that this is sufficiently larger for confined thin films (Bannenberg et al., 2016).

Differently, (de)hydrogenation can also occur more uniformly without the formation of large domains. This was found for example during desorption of the film studied by Mooij and Dam. Here, after desorption a porous film was also formed (Bannenberg et al., 2016; Mooij & Dam, 2013). It was then argued that the different mechanisms are induced by the large plastic deformation needed for absorption as the layer has to increase by 30% in thickness. As the film remains (at least for some time) porous, the re-hydrogenation of the film can therefore also occur much faster than the first hydrogenation.

3.4.1.3 Alloying

Alloying magnesium with elements such as Pd, Fe, Co, Ti, Mn, Ni, V and combinations thereof have also been considered as a way to improve both the kinetics and equilibrium thermodynamics (Crivello et al., 2016; Dornheim et al., 2007; Hitam et al., 2021; Lin et al., 2022; Ouyang et al., 2020; Schwarz, 1999; Zaluska et al., 1999). An example in which alloying turned out to be successful in enhancing the kinetics is in a Mg–Fe–Cr alloy. Here, it turns out that there is a catalytic effect of the alloy as the formation of a blocking β-MgD_2 layer is avoided. Based on neutron reflectometry data, a hydrogen gradient across the film was observed with a solubility of up to $Mg_{1-x-y}Fe_xCr_yH_{0.45}$ in the α-phase (Fritzsche et al., 2012). Differently, in Mg–Fe–V alloys it was suggested that Fe–V particles can act as nucleation sites and thereby enhance the kinetics (Zahiri et al., 2010).

Another way in which size and alloying affects can be combined is in the Mg–Ti system. Mg and Ti are practically immiscible. This results in the formation of a self-organised nanometre sized clusters of Mg that are coherently embedded in a Ti matrix with a larger surface-to-volume ratio as a result (Asano et al., 2015; Borsa et al., 2007). Also, other elements that are immiscible with magnesium have been considered, such as Mn (Lin et al., 2022; Lu et al., 2021). Similar to the case of Mg–Ti, here the size of the Mg domains can be controlled by the Mg–Mn ratio and an effective destabilisation of Mg was achieved, attributed to lattice distortion at the Mg–Mn interfaces. As such, this results in an effective destabilisation of the β-MgH_2 phase implying that hydrogen desorption can occur at lower temperatures (Lu et al., 2021). In addition, also high-entropy alloys have been employed to lower the thermodynamic stability of MgH_2 through inducing lattice strain and distortion (Asano et al., 2024).

3.4.1.4 Outlook

The study of magnesium thin films has resulted in important insights into the thermodynamical stability and hydrogen absorption and desorption kinetics. In particular, kinetic enhancement has often been achieved and for instance alloying has been a successful strategy in this. Destabilisation is more difficult to achieve, in particular in a way that can be used on the large scale needed for hydrogen strorage. One of the more promising methods is alloying with immiscible elements in which small destabilised Mg particles are formed. While for Mg–Ti this turned out to be more problematic, the Mg–Mn system turns out to have better prospects in bulk (Lu et al., 2019). Nevertheless, as the atomic fraction of Mg becomes relatively small, the effective hydrogen capacity is then also reduced substantially while production cost and weight are increased substantially.

3.4.2 Switchable mirrors

In the mid-90s, scientists discovered that a reversible metal-to-insulator transition can occur in rare-earth metal hydride thin films, such as the early discovered Y and La-

hydrides (Huiberts et al., 1996). As illustrated in Fig. 3.8, they found that while the dihydrides of these materials are shiny metals, the trihydrides - formed when exposing the dihydrides to a sufficiently high partial hydrogen pressure - are transparent. The idea was that such a large optical change can be used in a switchable mirror or a smart window. When transparency is required, the material can be exposed to hydrogen (either by gas loading or electrochemically) to get to the trihydride state, while a reflective state can be obtained when no exposure to hydrogen occurs, and the

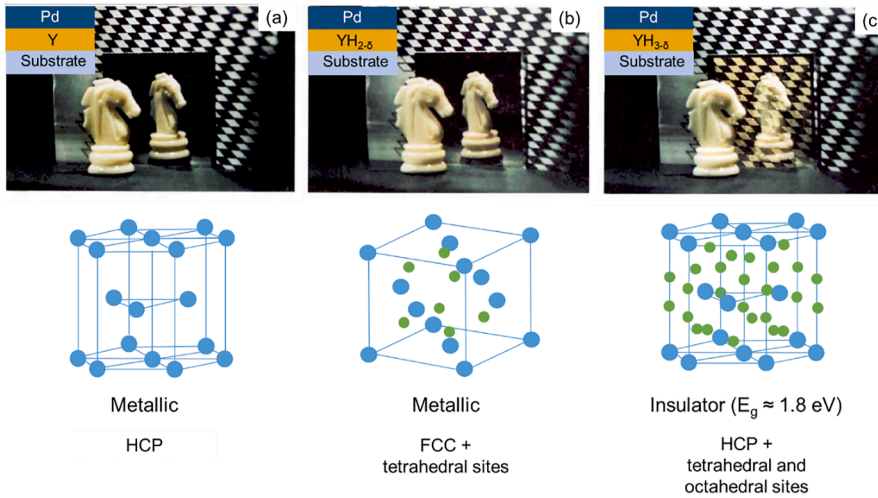


Figure 3.8 Schematic illustration of the working principle of a metal hydride switchable mirror. The figure shows a schematic illustration of a metal hydride switchable mirror using the example of a 500 nm Y film capped by a 20 nm thin film. In its original state, (a) yttrium, crystallising in a hexagonal closed packed structure, is metallic and thus reflects light. When exposed to a small partial hydrogen pressure, the dihydride phase is formed: a face centred cubic phase in which almost all tetrahedral sites are occupied by hydrogen leading to a hydrogen-to-metal ratio of just under 2. This transition is under room temperature irreversible, that is, if the hydrogen is removed from the environment the material remains in its $YH_{2-\delta}$ state. When the material is exposed to a higher hydrogen pressure, the 'trihydride' state can be formed. In this case the octahedral and tetrahedral sites of the hcp lattice are filled, yielding $YH_{3-\delta,}$ and the material becomes insulating with a bandgap of about $E_g = 1.8$ eV. The thin film becomes therefore transparent with a yellowish colour and the chess board can be seen through the film. When the hydrogen pressure is reduced, the material switches back to $YH_{2-\delta,}$ becomes metallic and thus reflective. The photographs were taken inside a glass tube that is filled with different partial hydrogen pressures. The chess piece is illuminated from the front and back to observe both the reflection and transmission of the light. The tetrahedral and octahedral sites are indicated by the green spheres; the yttrium atoms by blue spheres. Photographs adapted from Huiberts, J.N., Griessen, R., Rector, J.H., Wijngaarden, R. J., Dekker, J.P., de Groot, D.G., & Koeman, N.J. (1996). Yttrium and lanthanum hydride films with switchable optical properties. *Nature*, *380*(6571), 231-234. 10.1038/380231a0 with permission.

structure reverts back to the dihydride state. Ideally, for a smart window, one would block especially the infrared light and allow the passing of visible light. In this way, outward visibility can be maintained while heat inflow can be controlled, and less power needs to be provided to cool a building (Liang et al., 2019).

The materials first studied for these applications are trivalent rare-earth metal hydride thin films, which, when deposited as a metal, typically crystallise in a hcp structure. Upon exposure to hydrogen, an irreversible at moderate temperatures first-order phase transition occurs from the α-Y to the β-$YH_{2-\delta}$ phase, for Y at as low as $P_{H2} < 10^{-26}$ Pa at room temperature. In β-$YH_{2-\delta}$ forming a metallic state, the yttrium atoms form a face-centred cubic structure with the tetrahedral sites occupied by hydrogen atoms. When a larger hydrogen pressure is applied, around $P_{H2} = 10^{3}$ Pa, a first-order metal-to-insulator phase transition occurs from the β-$YH_{2-\delta}$ dihydride phase to the γ-$YH_{3-\delta}$ trihydride phase. In this latter phase, the yttrium atoms form a hexagonal structure and for the hydrogen atoms several arrangements have been proposed (Wolf & Herzig, 2002; Wolf & Herzig, 2003). Most importantly, γ-$YH_{3-\delta}$ is a semiconductor and therefore allows relatively high transparency of light. Different from the α-β transition, the β-γ is reversible, yet with a substantial hysteresis. To circumvent this, also fcc $YH_{3-\delta}$ has been synthesised by producing a nanocrystalline material with PLD (Lokhorst et al., 2003) or by partially substituting Y by Mg (Van der Molen et al., 2001). Also other rare earths such as La have a fcc trihydride state (Van Gogh et al., 2000). It is important to note that stochiometric YH_3 can only be formed under high pressures ($P_{H2} \approx 4$ GPa) and that in most cases a single phase that is typically formed with a sub-stoichiometric composition of $YH_{2.7}$ -$YH_{2.9}$ is observed (Kerssemakers et al., 2002; Remhof, 2002; Wolf & Herzig, 2002). It implies that hydrogen-vacancies can act as donors (Huiberts et al., 1997; Ng et al., 1997), and the material should thus behaves as a very heavily doped semiconductor (Huiberts et al., 1996; Ng et al., 1999). In a practical device, the rare-earths need to be combined with a thin capping layer made of e.g., Pd to promote the dissociation of hydrogen and prevent oxidation.

Although yttrium shows a reversible switching between a metallic (reflective) and semiconductor (transparent) states, for technological applications its properties are not ideal. One of the unwanted features is the yellow characteristic colour in the transparent state, which originates from the higher optical transmission for red light than for blue light. Such a characteristic colour can also be seen for other rare earth metal hydrides, such as red for La (Van Gogh et al., 2000) or yellowish red for Gd (Van der Sluis et al., 1997). For applications, one wants a colour-neutral highly transparent state and a much higher optical transmission than for YH_x, or effectively, a larger contrast between the reflective and transparent state. Furthermore, the large volumetric expansion (~10%) and hysteresis between the β-$YH_{2-\delta}$ and γ-$YH_{3-\delta}$ phases renders the material unstable for repetitive cycling.

As summarised in Table 3.1, to achieve these desired properties, one needs to find a material with a much larger bandgap while at the same time a similar/suitable enthalpy of formation of the trihydride state needs to be present to warrant the reversibly character of the β-$YH_{2-\delta}$ to γ-$YH_{3-\delta}$ phase transition (Van der Sluis et al., 1997). Magnesium was therefore a logical choice: magnesium hydride is optically transparent with a large

Table 3.1 List of desired functional properties of a switchable mirror and the relations to the structural properties of the material.

Functional property	Structural property
High transparency in transparent state	• Large optical transmission of the (capping) layer, • Thin capping layer
Colourless	• Large bandgap, • Constant optical transmission between $400 < \lambda < 800$ nm
Suitable switching pressures	• Suitable enthalpy/entropy of hydrogenation of the trihydride state, • No/limited hysteresis
Large amount of switching times	• No intermixing of layers, • No oxidation, • No large volumetric expansion from dihydride to trihydride phase, • No phase transitions
Fast switching time	• High hydrogen diffusivity, small thickness, and fast hydrogen dissociation of the capping layer

bandgap ($E_g = 5.8$ eV). Alloys of Gd–Mg, Sm–Mg, Lu–Mg, and Y–Mg show indeed such a colourless transparent state. Furthermore, it turns out that upon the first exposure of these alloy films to hydrogen, the material disproportionates into REH_x and MgH_x domains (Nagengast et al., 1999). It was suggested that this is due to the very high affinity (negative enthalpy) of REs for hydrogen, and these elements then form hydrogen bonds first with the result that it separates from the Mg that absorbs hydrogen at slightly higher pressures. This is an important result, as the Mg domains can (i) enhance the reflectivity of the switchable mirrors in the metallic state as, in contrast to REs, Mg completely dehydrogenates if the material is not exposed to hydrogen, (ii) the presence of Mg domains closes the small transmission window of the REH_2 phase, and (iii) MgH_2 domains increase the transmission in the transparent state owing to its lower light absorption coefficient. Furthermore, the formation of MgH_2 stabilises the fcc $YH_{3-\delta}$ state (Van der Molen et al., 2001). In addition, it was discovered that a black, i.e., highly absorbing, intermediate state can be realized when part of the Mg is hydrogenated to MgH_2 and Mg and MgH_2 domains coexist (Giebels et al., 2004).

Inspired by these findings, scientists also started to develop switchable mirrors without REs. Magnesium itself is not suitable owing to its sluggish kinetics at room temperature. Therefore, alloys with especially Ni such as Mg_2NiH_x but also Ca, Co, Fe, Mn, Ti, and V have all shown to display a reversible metal-to-insulator transition with reasonable kinetics at room temperature (Richardson et al., 2001; Richardson et al., 2002; Yamada et al., 2009; Yamada et al., 2012; Maiorov, 2020). In addition, transition metal oxides as TiO_2 are considered as alloyants (Liu et al., 2018, 2019). From an application perspective, these alloys have a mayor advantage as no rare earth is need anymore. However, the relatively low light transmission in the transparent state, typically below 1/3, and the rapid degradation of the material over repeated cycles prevent these materials from being applied in real devices.

Over the last decades, research focussed on solving these two problems. The limited light transmission in the 'transparent' state is at least in part caused by the capping layer, typically palladium, which remains metallic. As such, research into thinner or alternative materials was pursued to solve this with mixed results. Another problem, the rapid degradation caused by cycling between the reflective and transparent state, mainly originates from mixing between the different layers as well as blistering and cracking of the Pd layer (Bao et al., 2006, 2008; Yoshimura et al., 2007). To prevent this, intermediate layers such as Ti, Ta, NbO_x and AlO_x have been applied between the switchable mirror layer and the capping layer. A combination of a reduction of the Pd thickness to 3 nm and an intermediate Ta layer between the Pd and Mg–Y alloy resulted in over 10,000 successful cycles and a transmission of about 40% (Yamada et al., 2014).

While most studies have been using hydrogen gas loading, the ultimate application of the switchable metal hydride mirrors is likely based on electrochemical loading. In such an application, the metal-hydride layer (anode) is separated from a proton source layer (cathode) by a solid-state electrolyte and switching occurs by changing the potential between the proton source layer and the metal hydride layer. The idea is then that the inner side of double-glazed windows can then be coated with such a stack of layers (Armitage et al., 1999; Tajima et al., 2008, 2010).

The electrochemical switching has been explored in literature, for instance for Mg_2NiH_4. In this system, where Mg and Mg_2Ni domains coexist after the first exposure to hydrogen, two anodic reactions occur when the mirror is switched from the reflective to the transparent state:

(1) Mg_2Ni (reflective state) $+ 4H^+ + 4e^- = Mg_2NiH_4$ (transparent state)
(2) Mg (reflective state) $+ 2H^+ + 2e^- = MgH_2$ (transparent state)

Simultaneously, at the cathode, in this case H_xWO_3, the following reaction occurs:

(3) H_xWO_3 (reflective state) $= WO_3$ (transparent state) $+ xH^+ + xe^-$

As illustrated in Fig. 3.9, these two layers are separated by a Ta_2O_5 solid electrolyte that allows conduction of H^+ but is electronically insulating, an Al buffer layer to avoid mixing of the solid electrolyte with the Pd layer that promotes H^+ absorption into the Mg_2NiH_x layer. Switching can then be done by applying a voltage of $+/-5V$, changing within 5 seconds between a transparent ($\pm 40\%$ transmission) and reflective state (0% transmission) for at least 500 cycles. Even higher transmissions could be obtained by reducing the thickness of the Pd layer; however, this results in a rapid decay of the switchable mirror after only a limited number of cycles (Tajima et al., 2010).

3.4.2.1 Summary and outlook

Despite relatively good results, a major issue remains the relatively low transmission of the window in the transparent state, as well as the high production costs, which remain to date unresolved. Nevertheless, the concept of changing optical properties with exposure to hydrogen has inspired e.g., the development of optical transmission

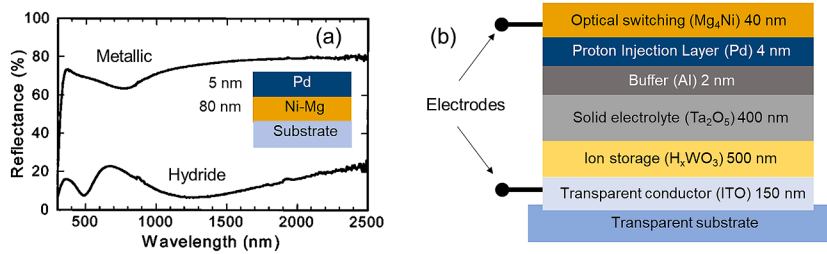


Figure 3.9 Example of a switchable mirror material and device. (a) Reflectance spectra of a 80 nm Ni–Mg film with 5 nm Pd capping layer on a glass substrate for both the metallic (upper curve) and hydride (lower curve). (b) Schematic illustration of an electrochemical switchable mirror that can be reversible switched between the transparent and reflective state by applying a voltage.
(a) Adapted with modifications from Richardson, T. J. et al. (2001). Switchable mirrors based on nickel–magnesium films. *Applied Physics Letters, 78*(20), 3047–3049, with permission. (b) Adapted from K. Tajima, K. et al. (2010). Fabrication study of proton injection layer suitable for electrochromic switchable mirror glass. *Thin Solid Films, 519*(2) (2010), 934–937 with permission.

measurement ('hydrogenography') as a tool for studying thin film metal hydrides and had a cross-over to the development of new metal-hydride hydrogen sensing materials.

3.4.3 Hydrogen sensors

Reliable, fast and efficient sensing of hydrogen forms an important ingredient for the future hydrogen economy. Hydrogen sensors can detect and quantify leaks of hydrogen, important for safety reasons as hydrogen-air mixtures can become flammable or even explosive when the hydrogen concentration exceeds 4% in air. On top of that, leaks should be detected to mitigate the emission of greenhouse gasses. Indeed, hydrogen itself is an indirect greenhouse gas with a CO_2 equivalent of 10–25 larger as it prolongs the lifetime of gasses such as methane (Derwent, 2023; Lakshmanan & Bhati, 2024; Ocko & Hamburg, 2022; Sand et al., 2023). In addition, hydrogen sensors can and are implemented to monitor fuel cells and electrolyzers and have (potential) application in a variety of industrial processes (Abe et al., 2019; Bakenne et al., 2016; Foorginezhad et al., 2021; Glenk & Reichelstein, 2019; Oliveira et al., 2021; Tashie-Lewis & Nnabuife, 2021). At present, hydrogen detection and sensing are performed with either catalytic, electrochemical, or thermal conductivity sensors (Hübert et al., 2018; Hübert et al., 2011). Although each of these sensors have their traits, neither of them fulfils all requirements in terms of sensing range (hydrogen concentration range that a senser can detect), resolution (accuracy of the sensor), response time, low-cost, cross-sensitivity to other gasses, operation in vacuum, amongst others.

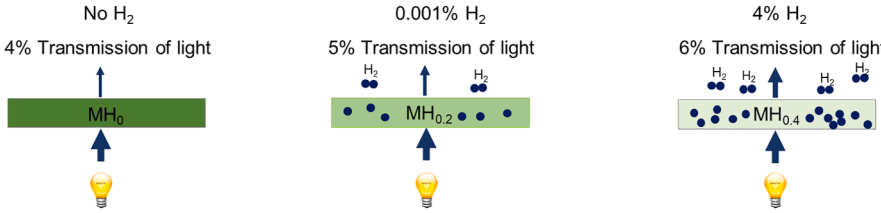


Figure 3.10 Schematic illustration of the working principle of metal hydride optical hydrogen sensors. When a metal hydride is exposed to an environment with no hydrogen present, no hydrogen is present in the metal M. This results in an exemplary transmission of 4% of the light. If the metal hydride is exposed to an environment containing hydrogen, let say 0.001%, hydrogen is absorbed by the metal hydride forming e.g., $MH_{0.2}$. This absorption of hydrogen by the metal changes the electronical and optical properties of the metal hydride, changing the transmission of the material to e.g., 5%. When the hydrogen concentration in the environment of the metal hydride thin film is further increased, more hydrogen is absorbed by the thin film, causing a larger change in the optical properties and thus a larger change in the transmission of the light.

Thin film metal hydrides have the potential to meet all these requirements in one sensor. As illustrated in Fig. 3.10, the working principle of these sensors is based on the fact that when exposed to an environment in which hydrogen is present, the metal hydride (typically a thin film or arrays of nanoparticles) would absorbs hydrogen. This causes a change in their electronic and optical properties, which can be probed by measuring properties such as the optical transmission, reflectivity, localised surface plasmon resonance, or the electrical conductivity. As the absorption of hydrogen by a metal hydride depends on temperature through Van 't Hoff's law, such a metal hydride sensor should always be combined with a temperature sensor to enable an accurate reading (Bannenberg et al., 2020; Chen et al., 2021; Darmadi, Nugroho, & Langhammer, 2020; Koo et al., 2020).

3.4.3.1 Hydrogen sensing materials

No matter whether the sensor relies on an electrical reading, or which type of optical readout mechanism is used (see Section 3.4.3.2), the sensing characteristics of a metal hydride hydrogen sensors are directly linked to the material properties of the metal hydride when exposed to hydrogen. Table 3.2 shows these connections: For example, to achieve a hysteresis free hydrogen sensor, i.e., a hydrogen sensor that is reversible and does not depend on the hydrogen pressure/concentration history, one should avoid first order phase transitions and plastic deformation caused by the absorption of hydrogen. To achieve a large sensing range, e.g., the pressure/concentration range in which the sensor is able to quantify the hydrogen pressure/concentration, a large solubility range within one phase (e.g., solid solution range) and a gradual change of the hydrogen-to-metal ratio with increasing hydrogen concentration/pressure in the atmosphere are required.

Table 3.2 List of characteristics of a hydrogen sensor and how they are related to the material properties.

Sensor characteristics	**Material property**
No hysteresis	- No first-order phase transition, no plastic deformation.
Large sensing range	- Gradual increase of the hydrogen-to-metal ratio of the material with changing hydrogen concentration, i.e., small dx/dP_{H_2} - large solubility range within one phase or within multiple phases with a second-order phase transition.
High sensitivity	- Large change of the hydrogen-to-metal ratio with changing hydrogen pressure/concentration. - Large change of the optical properties/resistance with changing hydrogen-to-metal ratio. - Optimal choice of the wavelength (for intensity modulated sensors)
Appropriate sensing range/ operating temperature	- Suitable enthalpy and entropy of hydrogenation.
Fast response	- High hydrogen diffusion coefficient. - Low amount of hydrogen absorbed. - Thin sensing layer. - High catalytic activity for the hydrogen dissociation reaction. - Use of surface coatings to lower hydrogen dissociation reaction's activation energy/keep surface clean.
Long lifetime	- Good adhesion between layer and substrate. - No plastic deformation; expansion due to hydrogen absorption is purely elastic. - No deactivation due to poisoning.
No cross-sensitivity	- Apply coatings to the sensing stack - Alloy the layer that has a hydrogen dissociative (catalytic) function with metals to make it resistant to chemical species.

Table 3.3 presents an overview of different classes of metal hydride materials that have been considered for hydrogen sensing. Roughly speaking, they can be divided into two groups: (i) materials that can both readily dissociate molecular hydrogen into atomic hydrogen and provide a change in optical properties/resistivity when exposed to hydrogen, i.e., Pd and Pd-alloys, and (ii) materials in which this hydrogen dissociation and sensing functionality is performed in a different layer. In the latter group, the material that provides the optical/resistivity contrast is a separate layer and combined with a top palladium(alloy) or another catalyst layer.

Palladium has by far been the most studied material. Since the original reports in the 1990s, palladium has been the material of choice for many studies. Indeed, it readily absorbs hydrogen at room temperature, provides a large contrast in optical properties/resistivity and it has a modest sensing range of about $0.1 < c_{H2} < 10\%$

Table 3.3 List of metal-hydride hydrogen sensing materials and their main characteristics.

Sensing material	Main characteristics
Palladium	• Can provide both an optical/resistivity contrast and dissociate molecular hydrogen into atomic hydrogen. • First order phase transition causing a highly hysteretic response. • Reversible (but with large hysteresis). • Operating temperature range up to about 90 °C. • Modest sensing range at room temperature. • Prone to delamination and cracking shortening lifetime. • Optical contrast around phase transition is large. • Response times can be long owing to the first order metal-to-metalhydride transition.
Palladium–gold and other palladium alloys (PdAuCu, PdNi, PdAg etc).	• Can provide both an optical/resistivity contrast and dissociate molecular hydrogen into atomic hydrogen. • First order phase transition of palladium suppressed when alloyant concentration is large enough (~15%–20% for Au depending on nanostructuring/confinement) • Reversible (but hysteresis may still be present for thin films even up to high % of Au owing to plastic deformation.) • Operating temperature range up to about 100 °C • Sensing range can be large, but sensitivity can vary across the sensing range. • Higher levels of alloyant substitution decreases hydrogen-to-metal ratio, causing lower magnitude of optical response and thus lower sensitivity. • Less prone to delamination and cracking as Pd. • Response times can be short (<1 second), especially in combination with a PTFE coating to reduce dissociation activation energy.
Tantalum and tantalum alloys	• Needs an additional catalytic layer (e.g., PdAu alloy) to dissociate molecular hydrogen into atomic hydrogen. • Completely free of hysteresis and reversible as no phase-transition occurs and a large solid-solution range of hydrogen and the host metal alloy is formed. • Operating temperature range up to at least 270 °C. • Large sensing range of over 7 orders of magnitude in hydrogen concentration/partial hydrogen pressure at RT. • Optical contrast and sensing range can be tuned by alloying with e.g., Ru or Pd. • Expansion is completely elastic, no problems with delamination or other stability problems observed. • Response times can be short (<1 second), especially in combination with a PTFE coating to reduce dissociation activation energy of the catalytic layer.

Table 3.3 Continued

Sensing material	Main characteristics
Hafnium	• Needs an additional catalytic layer (e.g., PdAu alloy) to dissociate molecular hydrogen into atomic hydrogen. • First time exposure to hydrogen causes an irreversible α-Hf – δ-$HfH_{1.6}$ phase transition. This transition becomes reversible at high temperatures ($T > 150$ °C) • Completely free of hysteresis and reversible as no first-order phase-transition occurs within sensing range and a large solid-solution range of hydrogen and the host metal alloy is formed $1.6 < x < 2.0$ in HfH_x. • Limited operating temperature range of around $90 < T < 150$ °C as the sensor saturates at too low hydrogen concentration at lower temperatures and the α-Hf – δ-$HfH_{1.6}$ becomes reversible. • Large sensing range of over 7 orders of magnitude in hydrogen concentration/partial hydrogen pressure within temperature range. • Response times can be short (<1 second), especially in combination with a PTFE coating to reduce dissociation activation energy of the catalytic layer.
Magnesium-alloys and Yttrium alloys	• Needs an additional catalytic layer (e.g., PdAu alloy) to dissociate molecular hydrogen into atomic hydrogen. • Large hysteresis, reversibility is poor and materials can at present in practice only be used as a one-time sensor. • Small but tuneable sensing range. • Optical contrast is large owing to metal-to-insulator transition. • Alloying of Mg with Ti, Ni or Ni–Zr or Y with Zr can tune the plateau pressure as well as changing the thickness. • Response times are long owing to the first-order phase transition.

in inert gas at room temperature (depending on read-out). While this makes it an attractive material, it has also some severe disadvantages. Below its critical temperature of 290 °C in bulk, a first order metal-to-metal hydride transition occurs for PdH_x. Combined with the hysteresis as a result of the plastic deformation of the material, this renders the response highly hysteretic. Furthermore, this transition causes a relatively sluggish absorption of hydrogen and is thus one of the causes of the relatively long response times. On top of that, palladium thin films are prone to delamination and microcracking, which compromise the long-term stability of the material. This problem can partly be resolved by using e.g., a thin Ti layer between the substrate and the Pd to promote the adhesion.

Alloying with elements including Au (Bannenberg, Nugroho, et al., 2019; Luong et al., 2021; Ma et al., 2023; Nugroho, Darmadi, et al., 2018; Nugroho, Eklund, et al., 2018; Nugroho et al., 2019, 2022; Tomeček et al., 2024; Wadell et al., 2015; Westerwaal et al., 2013), Ag (Dai et al., 2013; Luong et al., 2021; Sharma & Kim, 2017; Wang & Feng, 2007), Cu (Darmadi et al., 2019, 2021) and Ni (Cheng et al.,

1996; Du et al., 2020; Hughes et al., 1995; Lee et al., 2010; Strohfeldt et al., 2013; Yang et al., 2010), has been a widely employed strategy to improve the properties of palladium. With all these alloyants, the goal is to eliminate the first-order phase transition and suppress the critical temperature. Most of these elements form a solid solution with Pd over the entire substitution range and enlarge the unit cell of palladium. The result is that besides that the phase transition is suppressed for high enough alloyant concentration (15–20% for Au, depending on nanoconfinement), that the increase of the metal-to-hydrogen ratio (and thus the change in optical/electronic properties) becomes more gradual, and that the solubility of hydrogen in the Pd alloy at low hydrogen concentration/pressures is increased, enlarging the sensing range. Furthermore, the incorporation of Au improves the hydrogen dissociation functionality of Pd (Bannenberg, Boshuizen, et al., 2021; Namba et al., 2018). However, alloying palladium comes with a price: the maximum hydrogen-to-metal ratio of the material is reduced as the alloyants themselves typically do not form hydrides. This causes a decrease in the change of the optical properties or resistivity when exposed to hydrogen. On top of that, in thin films hysteresis remains typically present up to large alloyant concentrations. Differently, this is not the case in nanoparticles where stress can be released also in the in-plane direction (Bannenberg, Nugroho, et al., 2019). As such, especially palladium-gold(-copper) nanoparticles have shown exceptional performance in hydrogen sensing (Fig. 3.11a–c), having in an inert gas environment a sensing range from the ppm to 100% hydrogen concentration, sub-second response times and no hysteresis (Darmadi et al., 2021; Luong et al., 2021; Ma et al., 2023; Nugroho et al., 2019; Nugroho et al., 2022; Tomeček et al., 2024).

The combination of fast response times and a wide sensing range spanning seven orders of magnitude that is completely reversible and free of any hysteresis at room temperature can be realized with tantalum-based hydrogen sensing materials (Fig. 3.11e–f). At first glance, tantalum seems unsuitable for hydrogen sensing at room temperature. The bulk tantalum-hydrogen phase diagram shows that below a critical temperature of $T_c = 61$ °C a series of first-order phase transitions occur, which would imply a highly hysteretic response. However, the nanoconfinement of tantalum (see Section 11.2), ensures that these phase transitions are completely suppressed, even down to at least −60 °C (Bannenberg, Blom, et al., 2023; Yuan et al., 2025). This enables a large solid-solution range of tantalum and hydrogen spanning up to $TaH_{0.7}$. Furthermore, it turns out that while the hydrogen absorption by tantalum causes its bcc structure to deform considerably, this deformation and expansion is completely elastic, ensuring that the absorption/desorption of hydrogen is completely free of any hysteresis and allowing a long lifetime. These advantageous properties are directly translated into the sensing properties. Combined with a 10 nm catalyst PdAu (Cu) layer to promote the dissociation of hydrogen as well as 30 nm PTFE coating (Ngene, Westerwaal, et al., 2014), this material shows sub-second response times in an inert environment, a sensing range from ppm levels to 100% of H_2, complete reversibility and the absence of any hysteresis, and a wide range of operating temperatures: from −60–270 °C has meanwhile been demonstrated (Bannenberg, Schreuders, & Dam, 2021; Dewi et al., 2024; Yuan et al., 2025). Owing to the elastic nature of the expansion, stability to over 1000 loading-unloading cycles of hydrogen

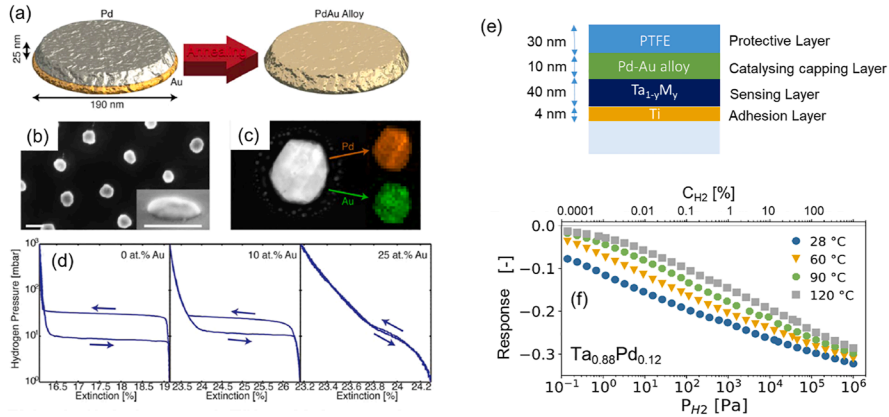


Figure 3.11 Examples of metal hydride hydrogen sensing materials. (a–d) show Pd and $Pd_{1-y}Au_y$ nanodisks. In these materials, the $Pd_{1-y}Au_y$ acts both as the catalyst for dissociating hydrogen from molecular to its atomic form and as a sensing layer, absorbing the hydrogen and providing the optical contrast. (a) Artist impression of the PdAu nanodisks made by hole-mask colloidal lithography and subsequent thermal annealing. (b) Scanning electron microscopy image of the nanoparticles (scale bar is 200 nm). (c) Scanning transmission electron microscopy image of the $Pd_{0.75}Au_{0.25}$ nanodisks together with compositional maps obtained from energy dispersive X-ray spectroscopy. (d) Hydrogen absorption and desorption isotherms at 30 °C for multiple compositions. The extinction is defined as the percentage of light absorbed by the sample in transmission at the localised surface plasmon resonance peak position. The higher the Au concentration, the smaller the hysteresis and optical changes become. (e)–(f) Tantalum based hydrogen sensing materials in which the hydrogen dissociation and hydrogen sensing functionality are separated into two layers. (e) Schematic illustration of the sensing stack. The $Pd_{0.6}Au_{0.4}$ layer catalyses the hydrogen dissociation, while the $Ta_{1-y}M_y$ layer provides the optical contrast, which can be tuned by alloying tantalum with e.g., Pd or Ru. (f) Example of the normalised change in optical transmission of a 40 nm $Ta_{0.88}Pd_{0.12}$ film capped with a 10 nm $Pd_{0.6}Au_{0.4}$ layer and with a 4 nm Ti adhesion layer. The response shifts with increasing temperatures to higher hydrogen concentrations/pressures. Figures (a)–(d) adapted from Wadell, C. et al. (2015). Hysteresis-free nanoplasmonic Pd-Au alloy hydrogen sensors. American Chemical Society, *Nano Letters, 15*(5), 3563–3570, Figure (f) adapted from Bannenberg, L., Schreuders, H., & Dam, B. (2021). Tantalum-Palladium: Hysteresis-Free optical hydrogen sensor over 7 orders of magnitude in pressure with sub-second response. *Advanced Functional Materials, 31*(16). https://doi.org/10.1002/adfm.202010483

has been demonstrated. Furthermore, the sensing properties can be further tuned by alloying Ta with elements including Pd (up to 12%) and Ru (up to 30%). These elements from a solid solution with tantalum but reduce the size of the unit cell. This ensures that the sensing range shifts to higher hydrogen concentrations (Griessen & Feenstra, 1985), allowing further control over the hydrogen sensing properties of the material (Bannenberg, Veeneman, et al., 2024; Bannenberg, Schreuders, & Dam, 2021; Bannenberg, Schreuders, et al., 2023; Ao et al., 2024).

Hafnium is another metal hydride that looks at first glance completely unsuitable for hydrogen detection but that turns out to provide a wide optical sensing range

spanning six orders of magnitude in hydrogen pressure (Bannenberg, Boelsma, et al., 2019; Boelsma and et al., 2017). The bulk hafnium-hydrogen phase diagram shows near room temperature three phases: a low-concentration hafnium hcp phase ($x < 0.05$), a fcc δ-HfH_x phase for $1.6 < x < 1.8$, and a face-centred-tetragonal ε-HfH_x phase for $1.9 < x < 2$ (Dottor, 2023; Mintz, 1996). Between these phases, first-order phase transitions occur involving phase coexistence, which would render the response of a hafnium-based sensor highly hysteretic. However, it turns out that for modest temperature (i.e., $T <\approx 150$ °C) that the α->δ transition is irreversible and that no phase coexistence or hysteresis occurs for the δ<−>ε phase transition (Bannenberg, Schreuders, & Dam, 2021). As such, when combined with a palladium cap layer reversible hydrogen sensing can occur in a relatively wide hydrogen-to-metal range of $1.6 < x < 2$, which spans around six orders of magnitude in hydrogen pressure at 120 °C, has a constant relative resolution and relatively fast response times. We note here that at these temperatures, the Pd capping layer only absorbs hydrogen for much larger pressures/concentration and its contribution to the total optical contrast can be neglected. One particular downside of hafnium as a sensing material is the limited operating temperature range. The combination of the enthalpy and entropy of hydrogenation makes it relatively favourable for hafnium to absorb large quantities of hydrogen at modest pressures. At 120 °C the material saturates with hydrogen already at 1 kPa/$c_{H2} = 1\%$, i.e., forming $HfH_{1.98}$. As such, no further change in the optical properties occur if the hydrogen pressure/concentration is increased beyond this value. Furthermore, this implies that for lower temperatures hafnium will, according to Van't Hoff's law, saturate at even lower hydrogen pressures, making it unsuitable for most applications at these working temperatures.

Magnesium and yttrium have also been investigated owing to the large change in optical properties when they absorb hydrogen. Indeed, both materials have a metal-to-insulator transition causing the optical transmission and resistivity to increase substantially: the transmission of a 40 nm thin film increase by about a factor 10, much larger than any of the aforementioned materials (e.g., 40 nm Pd: about 80% increase). Nevertheless, these materials have at least two major disadvantages: the optical changes occur at a well-defined plateau pressure and are associated with a first order phase transition, implying that hydrogen can be detected in a small pressure/concentration window with relatively slow kinetics. Furthermore, the hydrides are very stable, limiting reversibility of the sensor: it can only occur at very low partial hydrogen pressures and with very slow kinetics. Alloying Mg or Yttrium with Ti, Ni, or Zr has been employed to improve these properties, and these strategies can slightly widening/shifting the sensing range (Slaman et al., 2007; Palmisano et al., 2010; Radeva et al., 2014; Ngene, Radeva, et al., 2014; Victoria et al., 2016; Yoshimura et al., 2008; Ngene et al., 2017). The most eyeworthy application is that sensors can be made from these materials that can be read out by the naked eye. This is done using either the thickness dependence of the plateau pressure of a magnesium thin film (Palmisano et al., 2010), or the plateau pressure dependence of the Zr dopant concentration in Yttrium that change colour at a certain hydrogen concentration (Radeva et al., 2014; Ngene, Radeva, et al., 2014; Ngene et al., 2017).

3.4.3.2 Readout mechanisms

Roughly speaking, there are two main ways to turn a metal hydride into a hydrogen sensor: by detecting either changes of the resistivity, or by measuring changes of optical properties. Resistivity sensors already exist since the 1970s when a thin film of palladium was measured using a four-probe resistance measurement (Fig. 3.12a). When palladium is exposed to a hydrogen containing environment, the palladium absorbs hydrogen, and the resistivity of the film goes up. Recently, more advanced geometries including patterned nanosheets, nanowires microelectromechanical systems have been considered for hydrogen sensing resulting in larger sensitivities (Hübert et al., 2011; Koo et al., 2020).

Optical hydrogen sensors feature three inherent advantages over hydrogen sensors with an electrical readout: They do not require electrical leads near the sensing area, a key safety benefit, they are less prone to electromagnetic radiation, and a wealth of information can be detected as each wavelength of light can show a different response to hydrogen, allowing more accurate measurements. The optical hydrogen sensors can be divided into intensity modulated and frequency modulated hydrogen sensors. Although not always true, typically intensity modulated sensors are simpler to manufacture but are more prone to fluctuations of the light source/vibrations, while frequency modulated sensors require more advanced and expensive components but are inherently not sensitive to fluctuations of the light source's intensity.

Intensity modulated sensors measure the change in optical reflection or transmission of a metal hydride. This can be as simple as measuring the transmission or reflectivity of a thin film when it is exposed to an environment containing hydrogen. In such a configuration, a LED light source can be used in combination with a photodiode (Fig. 3.12b). Alternatively, one can create a micro-mirror hydrogen sensor by depositing the metal hydride on the tip of an optical fibre (Fig. 3.12c) (Butler, 1994; Verhoeff et al., 2025; Westerwaal et al., 2013; Zhang et al., 2017). Light, originating from e.g., an LED light source, is then coupled into the fibre and reflected by the metal hydride layer. This light can then be detected by a photodiode. If the hydrogen concentration changes, the reflectivity of the metal hydride changes. As a result, the measured light intensity changes which can be converted into a hydrogen concentration. Although such a sensor is typically prone for fluctuations of the light source, one can use the wavelength-dependence of these reflectivity changes to accurately discriminate between drifting light sources and changing hydrogen concentration (Bannenberg, 2023).

Although many more types of frequency modulated sensors exists, two popular ones include sensors based on fibre-Bragg gratings (FBG) and on (localised) surface plasmon resonance (LSPR). The basic form of an FBG sensor consist of an optical fibre in which the core contains a grating composed of alternating materials of different refractive indexes. On the cladding, the material surrounding the core, resp. of the optical fibre, a metal hydride layer is deposited (Fig. 3.12d). This fibre then reflects only light with one specific wavelength, depending on the period of the grating. When the FBG sensor is exposed to hydrogen, the metal hydride absorbs it, causing it to expand. This changes the period of the grating, shifting the wavelength

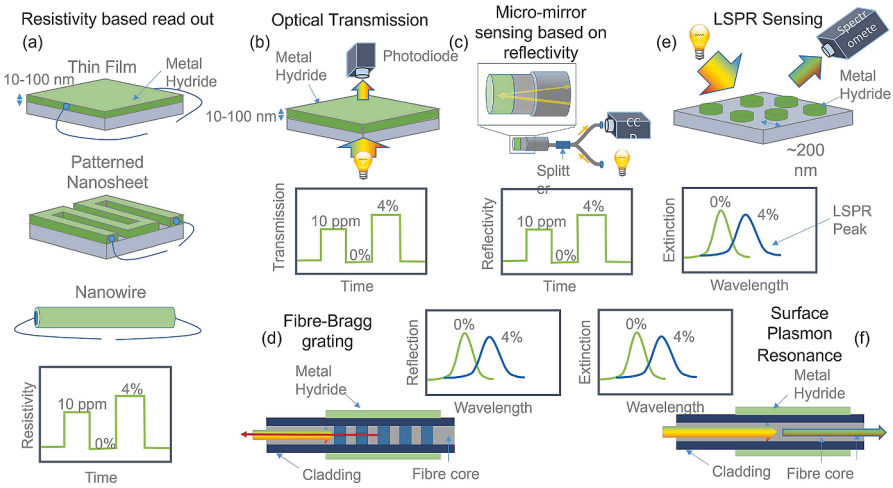


Figure 3.12 Examples of metal hydride hydrogen sensor readout mechanisms. (a) Resistivity based sensors measure changes in the electrical resistivity/conductivity of e.g., a metal thin film to determine the hydrogen concentration/pressure. (b–f) In optical based sensors, the intensity or frequency of the transmitted/reflected light is measured as a function of time. (b) In an optical transmission sensor, a change in hydrogen concentration is translated in a change in the optical transmission. (c) In a micro-mirror sensor, the metal hydride sensing layer is deposited at the end of an optical fibre. Light is then coupled into the fibre and partially reflected by the metal hydride layer. The intensity of the reflected light is then monitored by a photodiode or charged-coupled device (CCD). (d) In a fibre-Bragg grating, white light is coupled into an optical fibre in which a grating is present. This grating precisely reflects one wavelength of the light. On the side of the fibre at the position of the grating, a metal hydride is applied. When hydrogen is absorbed, the metal hydride expands and the periodicity of the grating changes. This changes the wavelength that is reflected by the grating. (e) In a localised surface plasmonic resonance (LSPR) sensor, metal hydride nanoparticles are illuminated by white light. Then, the transmission or reflection spectrum of this light is monitored. In this spectrum, a 'dip' is visible, which results to absorption of light by surface plasmons. Typically, the extinction is plotted instead of the transmission, and a LSPR peak is observed. This peak shifts and changes shape when the metal hydride absorbs hydrogen in response to a changing hydrogen concentration. (f) A similar technique is the surface plasmon resonance, in which a coating is applied on the side of an optical fibre. At the SPR wavelength, a dip is seen in the optical transmission, or equivalently, a maximum in the extinction spectrum. This maximum shift if hydrogen is absorbed by the metal hydride.

that is reflected. By detecting the wavelength shift, the hydrogen concentration in the vicinity of the sensor can then be measured (Trouillet et al., 2006; Dai et al., 2012; Coelho et al., 2015; Ping et al., 2024; Dai et al., 2013; Fisser et al., 2018). Alternatively, one can use more advanced FBGs as for instance tilted-FBG to be sensitive to changes in the dielectric properties of the metal hydride (Dissanayake et al., 2024; Ping et al., 2024; Zhang et al., 2022).

Surface plasmon hydrogen sensors rely on the excitation of plasmon resonance by the incoming light. When light illuminates a material, it may be absorbed if the frequency/wavelength of the light matches with the plasmon resonance frequency. This plasmon resonance frequency depends on the dimensions and dielectric constants of the material. If such a material absorbs hydrogen, the plasmon resonance frequency changes, leading to a different (band of) frequencies to be partly absorbed. SPR sensors can be designed in multiple ways. In one way (Fig. 3.12e), a metal hydride is deposited on the side of an optical fibre and SPR effect may occur between the interface of this metal layer and the dielectric medium on which it is deposited. Then, if designed correctly, a dip in the transmission spectrum of the fibre occurs. Instead of plotting the transmission, commonly the light extinction is plotted, and this 'dip' becomes visible as a 'peak'. Upon exposure to hydrogen, this SPR peak will shift (Bévenot et al., 2002; Hosoki et al., 2013; Kim et al., 2022; Perrotton et al., 2013). An alternative method is to fabricate nanoparticles of metal hydrides. In this case, the particles are typically smaller than the wavelength of the incident light, leading to strong absorption and scattering effects when the incident light matches the localised SPR frequency shows a strong dependence on the size, shape and dielectric properties of the nanoparticle. This can then be probed by measuring either the transmission or reflectivity of an array of such nanoparticles (Ai et al., 2022; Darmadi et al., 2021; Sterl et al., 2020; Wadell et al., 2014).

3.4.3.3 Summary and outlook

Over the past years, metal-hydride optical hydrogen sensors have been developed focussing on parameters including sensing range, response time, sensitivity, and stability. In particular, hydrogen sensors based on Pd–Au alloys and tantalum-alloys demonstrate sensing ranges from ppm to 100% hydrogen concentration at room temperature that are reversible and free of any hysteresis.

While these are fantastic traits, most of these measurements have been performed under relatively ideal conditions. It is known that the presence of other chemical species such as CO, NO_x, H_2S, SO_x can affect the performance of the sensors, both in terms of response time and response magnitude. Especially the latter is problematic, as it implies that there is no unambiguous relation between the readout of the sensor and the actual hydrogen concentration. To mitigate this, especially polymer coatings have been developed. Poly(methylmethacrylate) (PMMA) and polytetrafluoroethylene (PTFE) are two to highlight. PMMA has shown to provide good protection against CO, CO_2 and NO_2 (Chen et al., 2021; Darmadi et al., 2020; Hong et al., 2015; Nugroho et al., 2019), while PTFE provides some protection but also has the major advantage that it can accelerate the hydrogenation kinetics substantially up to a factor of 10 (Ngene, Radeva, et al., 2014; Nugroho et al., 2019; Bannenberg, Schreuders, & Dam, 2021; Darmadi et al., 2023). Two mechanisms have been proposed: one is that the PTFE keeps the surface cleaner, ensuring that more active sites remain available for the hydrogen dissociation. The other mechanism is that PTFE, forming bonds with the Pd layer underneath has been found to reduce the activation energy of the hydrogen dissociation reaction, and in this way accelerates the kinetics

significantly. Another approach is to make the Pd-based sensing or catalyst layer more resistive to poisoning, e.g., CO resistance has been achieved by introducing Cu in a PdAu layer (Darmadi et al., 2019).

Another outstanding problem to tackle is measurements under high humidity. Humidity has been addressed by various studies, but rarely up to 95% RH or even fully condensing atmospheres. This is especially relevant for applications inside/near electrolysers and fuel cells. Furthermore, the integration into real prototype/commercial sensors is a way to go forward.

References

Abe, J. O., Popoola, A. P. I., Ajenifuja, E., & Popoola, O. M. (2019). Hydrogen energy, economy and storage: Review and recommendation. *International Journal of Hydrogen Energy, 44*(29), 15072–15086. https://doi.org/10.1016/j.ijhydene.2019.04.068

Ai, B., Sun, Y., & Zhao, Y. (2022). Plasmonic hydrogen sensors. *Small, 18*(25). https://doi.org/10.1002/smll.202107882

Andersson, G., Hjörvarsson, B., & Zabel, H. (1997). Hydrogen-induced lattice expansion of vanadium in a Fe/V (001) single-crystal superlattice. *Physical Review B, 55*(23), 15905–15911. https://doi.org/10.1103/physrevb.55.15905

Ao, W., Xue, B., Dai, J., Hu, W., Zhang, F., & Yang, M. (2024). Pd–Ta alloy films hydrogen sensors based on partially coated π-phase-shifted FBG. *Optical Materials, 152*, 115476. https://doi.org/10.1016/j.optmat.2024.115476

Armitage, R., Rubin, M., Richardson, T., O'Brien, N., & Chen, Y. (1999). Solid-state gadolinium–magnesium hydride optical switch. *Applied Physics Letters, 75*(13), 1863–1865. https://doi.org/10.1063/1.124853

Asano, K., Bannenberg, L. J., Schreuders, H., Hashimoto, H., Isobe, S., Nakahira, Y., Machida, A., Kim, H., & Sakaki, K. (2024). Distortion and destabilization of Mg hydride facing high entropy alloy matrix. *ACS Applied Energy Materials, 7*(24), 11644–11651. https://doi.org/10.1021/acsaem.4c02569

Asano, K., Westerwaal, R. J., Anastasopol, A., Mooij, L. P. A., Boelsma, C., Ngene, P., Schreuders, H., Eijt, S. W. H., & Dam, B. (2015). Destabilization of Mg hydride by self-organized nanoclusters in the immiscible Mg-Ti system. *Journal of Physical Chemistry C, 119*(22), 12157–12164. https://doi.org/10.1021/acs.jpcc.5b02275

Bévenot, X., Trouillet, A., Veillas, C., Gagnaire, H., & Clément, M. (2002). Surface plasmon resonance hydrogen sensor using an optical fibre. *Measurement Science and Technology, 13*(1), 118–124. https://doi.org/10.1088/0957-0233/13/1/315

Bakenne, A., Nuttall, W., & Kazantzis, N. (2016). Sankey-Diagram-based insights into the hydrogen economy of today. *International Journal of Hydrogen Energy, 41*(19), 7744–7753. https://doi.org/10.1016/j.ijhydene.2015.12.216

Baldi, A., & Dam, B. (2011). Thin film metal hydrides for hydrogen storage applications. *Journal of Materials Chemistry, 21*(12), 4021–4026. https://doi.org/10.1039/c0jm03249b

Baldi, A., Gonzalez-Silveira, M., Palmisano, V., Dam, B., & Griessen, R. (2009). Destabilization of the Mg-H system through elastic constraints. *Physical Review Letters, 102*(22). https://doi.org/10.1103/physrevlett.102.226102

Baldi, A., Mooij, L., Palmisano, V., Schreuders, H., Krishnan, G., Kooi, B. J., Dam, B., & Griessen, R. (2018). Elastic versus alloying effects in Mg-based hydride films. *Physical Review Letters, 121*(25), 10797114. https://doi.org/10.1103/PhysRevLett.121.255503

Baldi, A., Narayan, T. C., Koh, A. L., & Dionne, J. A. (2014). In situ detection of hydrogen-induced phase transitions in individual palladium nanocrystals. *Nature Materials, 13* (12), 1143–1148. https://doi.org/10.1038/nmat4086

Bannenberg, L. J. (2023). Algorithm to suppress drift for micromirror and other intensity-modulated hydrogen sensors. *IEEE Sensors Journal, 23*(24), 30720–30727. https://doi.org/10.1109/JSEN.2023.3328642

Bannenberg, L. J., Blom, L., Sakaki, K., Asano, K., & Schreuders, H. (2023). Completely elastic deformation of hydrogenated Ta thin films. *ACS Materials Letters, 5*(4), 962–969. https://doi.org/10.1021/acsmaterialslett.3c00038

Bannenberg, L. J., Boelsma, C., Asano, K., Schreuders, H., & Dam, B. (2020). Metal hydride based optical hydrogen sensors. *Journal of the Physical Society of Japan, 89*(5), 051003. https://doi.org/10.7566/jpsj.89.051003

Bannenberg, L. J., Boelsma, C., Schreuders, H., Francke, S., Steinke, N. J., van Well, A. A., & Dam, B. (2019). Optical hydrogen sensing beyond palladium: Hafnium and tantalum as effective sensing materials. *Sensors and Actuators B: Chemical, 283*, 538–548. https://doi.org/10.1016/j.snb.2018.12.029

Bannenberg, L. J., Boshuizen, B., Ardy Nugroho, F. A., & Schreuders, H. (2021). Hydrogenation kinetics of metal hydride catalytic layers. *ACS Applied Materials and Interfaces, 13* (44), 52530–52541. https://doi.org/10.1021/acsami.1c13240

Bannenberg, L. J., Bresser, R., van der Ende, P., van Exter, M., van Goozen, W., Naastepad, F., Thijs, M. A., Verleg, M. N., de Vroege, K., Waaijer, R., & van Well, A. A. (2023). The completely renewed and upgraded neutron reflectometer at the TU Delft Reactor Institute. *Review of Scientific Instruments, 94*(11). https://doi.org/10.1063/5.0155888

Bannenberg, L. J., Nugroho, F. A. A., Schreuders, H., Norder, B., Trinh, T. T., Steinke, N. J., Van Well, A. A., Langhammer, C., & Dam, B. (2019). Direct comparison of PdAu alloy thin films and nanoparticles upon hydrogen exposure. *ACS Applied Materials and Interfaces, 11*(17), 15489–15497. https://doi.org/10.1021/acsami.8b22455

Bannenberg, L., Schreuders, H., & Dam, B. (2021). Tantalum-Palladium: Hysteresis-Free optical hydrogen sensor over 7 orders of magnitude in pressure with sub-second response. *Advanced Functional Materials, 31*(16). https://doi.org/10.1002/adfm.202010483

Bannenberg, L. J., Schreuders, H., van Beugen, N., Kinane, C., Hall, S., & Dam, B. (2023). Tuning the properties of thin-film TaRu for hydrogen-sensing applications. *ACS Applied Materials and Interfaces, 15*(6), 8033–8045. https://doi.org/10.1021/acsami.2c20112

Bannenberg, L. J., Schreuders, H., Van Eijck, L., Heringa, J. R., Steinke, N. J., Dalgliesh, R., Dam, B., Mulder, F. M., & Van Well, A. A. (2016). Impact of nanostructuring on the phase behavior of insertion materials: The hydrogenation kinetics of a magnesium thin film. *Journal of Physical Chemistry C, 120*(19), 10185–10191. https://doi.org/10.1021/acs.jpcc.6b02302

Bannenberg, L. J., van Exter, M., Verleg, M. N., Boshuizen, B., Parnell, S. R., Thijs, M., & Schreuders, H. (2024). Versatile pressure and temperature controlled cell for neutron reflectometry and small-angle neutron scattering. *Journal of Neutron Research, 26*(1), 1–13. https://doi.org/10.3233/jnr-230004

Bannenberg, L. J., Verhoeff, D. J., Jonckers Newton, N., Thijs, M., & Schreuders, H. (2024). Structural and optical properties of thin film β-Ta upon exposure to hydrogen to asses its applicability as hydrogen sensing material. *ACS Applied Nano Materials, 7*(2), 1757–1766. https://doi.org/10.1021/acsanm.3c04902

Bao, S., Tajima, K., Yamada, Y., Okada, M., & Yoshimura, K. (2008). Metal buffer layer inserted switchable mirrors. *Solar Energy Materials and Solar Cells, 92*(2), 216–223. https://doi.org/10.1016/j.solmat.2007.02.023

Bao, S., Yamada, Y., Okada, M., & Yoshimura, K. (2006). Titanium-buffer-layer-Inserted switchable mirror based on Mg–Ni alloy thin film. *Japanese Journal of Applied Physics, 45*(6L), Article L588. https://doi.org/10.1143/jjap.45.l588

Björck, M., & Andersson, G. (2007). GenX : An extensible X-ray reflectivity refinement program utilizing differential evolution. *Journal of Applied Crystallography, 40*(6), 1174–1178. https://doi.org/10.1107/s0021889807045086

Bloch, J., Pejova, B., Jacob, J., & Hjörvarsson, B. (2010). Hydrogen-vanadium system in thin films: Effect of film thickness. *Physical Review B: Condensed Matter and Materials Physics, 82*(24). https://doi.org/10.1103/PhysRevB.82.245428Sweden

Boelsma, C., et al. (2017). Hafnium—an optical hydrogen sensor spanning six orders in pressure. *Nature Communications, 8*(1), 15718. https://doi.org/10.1038/ncomms15718

Borgschulte, A., Westerwaal, R., Rector, J., Schreuders, H., Dam, B., & Griessen, R. (2006). Catalytic activity of noble metals promoting hydrogen uptake. *Journal of Catalysis, 239*(2), 263–271. https://doi.org/10.1016/j.jcat.2006.01.031

Borsa, D. M., Gremaud, R., Baldi, A., Schreuders, H., Rector, J. H., Kooi, B., Vermeulen, P., Notten, P. H. L., Dam, B., & Griessen, R. (2007). Structural, optical, and electrical properties of $Mg_y Ti_{1-y} Hx$ thin films. *Physical Review B: Condensed Matter and Materials Physics, 75*(20). https://doi.org/10.1103/PhysRevB.75.205408

Bucur, R. V., Mecea, V., & Flanagan, T. B. (1976). The kinetics of hydrogen (deuterium) sorption by thin palladium layers studied with a piezoelectric quartz crystal microbalance. *Surface Science, 54*(2), 477–488. https://doi.org/10.1016/0039-6028(76)90238-7

Burlaka, V., Wagner, S., Hamm, M., & Pundt, A. (2016). Suppression of phase transformation in Nb–H thin films below switchover thickness. *Nano Letters, 16*(10), 6207–6212. https://doi.org/10.1021/acs.nanolett.6b02467

Butler, M. A. (1994). Micromirror optical-fiber hydrogen sensor. *Sensors and Actuators: B. Chemical, 22*(2), 155–163. https://doi.org/10.1016/0925-4005(94)87015-2

Bylin, J., Lindblad, R., Spode, L., Scheicher, R. H., & Pálsson, G. K. (2024). The influence of hydrogen on the electronic structure in transition metallic glasses. *arXiv*. https://doi.org/10.48550/arXiv.2403.13371

Chen, K., Yuan, D., & Zhao, Y. (2021). Review of optical hydrogen sensors based on metal hydrides: Recent developments and challenges. *Optics and Laser Technology, 137*, Article 106808. https://doi.org/10.1016/j.optlastec.2020.106808

Cheng, Y. T., Li, Y., Lisi, D., & Wang, W. M. (1996). Preparation and characterization of Pd/Ni thin films for hydrogen sensing. *Sensors and Actuators, B: Chemical, 30*(1), 11–16. https://doi.org/10.1016/0925-4005(95)01734-D

Cho, Y. J., Cho, H., & Cho, E. S. (2023). Nanointerface engineering of metal hydrides for advanced hydrogen storage. *Chemistry of Materials, 35*(2), 366–385. https://doi.org/10.1021/acs.chemmater.2c02628

Coelho, L., de Almeida, J. M. M. M., Santos, J. L., & Viegas, D. (2015). Fiber optic hydrogen sensor based on an etched Bragg grating coated with palladium. *Applied Optics, 54*(35), 10342–10348. https://doi.org/10.1364/AO.54.010342

Crivello, J.-C., Dam, B., Denys, R. V., Dornheim, M., Grant, D. M., Huot, J., Jensen, T. R., de Jongh, P., Latroche, M., Milanese, C., Milčius, D., Walker, G. S., Webb, C. J., Zlotea, C., & Yartys, V. A. (2016). Review of magnesium hydride-based materials: Development and optimisation. *Applied Physics A, 122*(2). https://doi.org/10.1007/s00339-016-9602-0

Cui, J., Wang, H., Liu, J., Ouyang, L., Zhang, Q., Sun, D., Yao, X., & Zhu, M. (2013). Remarkable enhancement in dehydrogenation of MgH_2 by a nano-coating of multi-valence Ti-based catalysts. *Journal of Materials Chemistry A, 1*(18), 5603–5611. https://doi.org/10.1039/c3ta01332d

Dai, J., Yang, M., Yu, X., Cao, K., & Liao, J. (2012). Greatly etched fiber Bragg grating hydrogen sensor with Pd/Ni composite film as sensing material. *Sensors and Actuators B: Chemical, 174*, 253–257. https://doi.org/10.1016/j.snb.2012.07.018

Dai, J., Yang, M., Yu, X., & Lu, H. (2013). Optical hydrogen sensor based on etched fiber Bragg grating sputtered with Pd/Ag composite film. *Optical Fiber Technology, 19*(1), 26–30. https://doi.org/10.1016/j.yofte.2012.09.006

Darmadi, I., Khairunnisa, S. Z., Tomeček, D., & Langhammer, C. (2021). Optimization of the composition of PdAuCu ternary alloy nanoparticles for plasmonic hydrogen sensing. *ACS Applied Nano Materials, 4*(9), 8716–8722. https://doi.org/10.1021/acsanm.1c01242

Darmadi, I., Nugroho, F. A. A., Kadkhodazadeh, S., Wagner, J. B., & Langhammer, C. (2019). Rationally designed PdAuCu ternary alloy nanoparticles for intrinsically deactivation-resistant ultrafast plasmonic hydrogen sensing. *ACS Sensors, 4*(5), 1424–1432. https://doi.org/10.1021/acssensors.9b00610

Darmadi, I., Nugroho, F. A. A., & Langhammer, C. (2020). High-performance nanostructured palladium-based hydrogen sensors - current limitations and strategies for their mitigation. *ACS Sensors, 5*(11), 3306–3327. https://doi.org/10.1021/acssensors.0c02019.

Darmadi, I., Östergren, I., Lerch, S., Lund, A., Moth-Poulsen, K., Müller, C., & Langhammer, C. (2023). Bulk-processed plasmonic plastic nanocomposite materials for optical hydrogen detection. *Accounts of Chemical Research, 56*(13), 1850–1861. https://doi.org/10.1021/acs.accounts.3c00182

de Man, S., Gonzalez-Silveira, M., Visser, D., Bakker, R., Schreuders, H., Baldi, A., Dam, B., & Griessen, R. (2013). Combinatorial method for direct measurements of the intrinsic hydrogen permeability of separation membrane materials. *Journal of Membrane Science, 444*, 70–76. https://doi.org/10.1016/j.memsci.2013.04.054

Derwent, R. G. (2023). Global warming potential (GWP) for hydrogen: Sensitivities, uncertainties and meta-analysis. *International Journal of Hydrogen Energy, 48*(22), 8328–8341. https://doi.org/10.1016/j.ijhydene.2022.11.219

Dewi, H. S., Dissanayake, K. P., Schreuders, H., Groves, R. M., & Bannenberg, L. J. (2024). Metal hydride hydrogen sensing materials from 28 °C to 270 °C. *International Journal of Hydrogen Energy, 84*, 606–614. https://doi.org/10.1016/j.ijhydene.2024.08.128

Di Vece, M., & Kelly, J. J. (2003). Electrochemical study of hydrogen diffusion in yttrium hydride switchable mirrors. *Journal of Alloys and Compounds, 356–357*, 156–159. https://doi.org/10.1016/s0925-8388(02)01225-2

Dissanayake, K. P. W., Dewi, H. S., Schreuders, H., Bannenberg, L. J., & Groves, R. M. (2024). *Design of a metal hydride-coated tilted fibre Bragg grating-based hydrogen sensor*. In Optical Sensing and Detection VIII. https://doi.org/10.1117/12.3016505

Dornheim, M., Doppiu, S., Barkhordarian, G., Boesenberg, U., Klassen, T., Gutfleisch, O., & Bormann, R. (2007). Hydrogen storage in magnesium-based hydrides and hydride composites. *Scripta Materialia, 56*(10), 841–846. https://doi.org/10.1016/j.scriptamat.2007.01.003

Dornheim, M., Pundt, A., Kirchheim, R., Molen, S. J.v.d., Kooij, E. S., Kerssemakers, J., Griessen, R., Harms, H., & Geyer, U. (2003). Stress development in thin yttrium films on hard substrates during hydrogen loading. *Journal of Applied Physics, 93*(11), 8958–8965. https://doi.org/10.1063/1.1568153

Dottor, M. (2023). Experimental determination of the H–Hf phase diagram using in situ neutron diffraction. *Journal of Alloys and Compounds, 937*, 168353. https://doi.org/10.1016/j.jallcom.2022.168353

Du, L., Feng, D., Xing, X., Wang, C., Armatas, G. S., & Yang, D. (2020). Uniform palladium-nickel nanowires arrays for stable hydrogen leakage detection and efficient hydrogen evolution reaction. *Chemical Engineering Journal, 400*. https://doi.org/10.1016/j.cej.2020.125864

Dura, J. A., Rus, E. D., Kienzle, P. A., & Maranville, B. B. (2017). *Nanolayer analysis by neutron reflectometry nanolayer research: Methodology and Technology for green chemistry* (pp. 155–202). United States: Elsevier Inc..

Dyck, A., Böhlke, T., Pundt, A., & Wagner, S. (2024). Phase transformation in the Niobium Hydrogen system: Effects of elasto-plastic deformations on phase stability predicted by a thermodynamic model. *Scripta Materialia, 251*. https://doi.org/10.1016/j.scriptamat.2024.116209

El Far, R., Diaz-Droguett, D. E., Rojas, S., Avila, J. I., Romero, C. P., Lievens, P., & Cabrera, A. L. (2012). Quantitative determination of hydrogen absorption by Pd cluster-assembled films using a quartz crystal microbalance. *Thin Solid Films, 522*, 199–203. https://doi.org/10.1016/j.tsf.2012.08.006

Feenstra, R., De Bruin-Hordijk, G. J., Bakker, H. L. M., Griessen, R., & De Groot, D. G. (1983). Critical point lowering in thin PdH_x films. *Journal of Physics F: Metal Physics, 13*(2), L13. https://doi.org/10.1088/0305-4608/13/2/001

Fisser, M., Badcock, R. A., Teal, P. D., Janssens, S., & Hunze, A. (2018). Palladium-based hydrogen sensors using fiber bragg gratings. *Journal of Lightwave Technology, 36*(4), 850–856. https://doi.org/10.1109/JLT.2017.2713038

Flanagan, T. B., & Oates, W. A. (1991). The palladium-hydrogen system. *Annual Review of Materials Science, 21*(1), 269–304. https://doi.org/10.1146/annurev.ms.21.080191.001413

Foorginezhad, S., Mohseni-Dargah, M., Falahati, Z., Abbassi, R., Razmjou, A., & Asadnia, M. (2021). Sensing advancement towards safety assessment of hydrogen fuel cell vehicles. *Journal of Power Sources, 489*, Article 229450. https://doi.org/10.1016/j.jpowsour.2021.229450

Fritzsche, H., & Huot, J. (2016). *Neutron scattering and other nuclear techniques for hydrogen in materials*, (pp. 115–118). Springer International Publishing.

Fritzsche, H., Kalisvaart, W. P., Zahiri, B., Flacau, R., & Mitlin, D. (2012). The catalytic effect of Fe and Cr on hydrogen and deuterium absorption in Mg thin films. *International Journal of Hydrogen Energy, 37*(4), 3540–3547. https://doi.org/10.1016/j.ijhydene.2011.06.014

Fukai, Y. (2006). *The metal-hydrogen system: Basic bulk properties*. Springer Science and Business Media.

Giebels, I. A. M. E., Isidorsson, J., & Griessen, R. (2004). Highly absorbing black Mg and rare-earth-Mg switchable mirrors. *Physical Review B, 69*(20). https://doi.org/10.1103/physrevb.69.205111

Glavic, A., & Björck, M. (2022). GenX 3 : The latest generation of an established tool. *Journal of Applied Crystallography, 55*(4), 1063–1071. https://doi.org/10.1107/s1600576722006653

Glenk, G., & Reichelstein, S. (2019). Economics of converting renewable power to hydrogen. *Nature Energy, 4*(3), 216–222. https://doi.org/10.1038/s41560-019-0326-1

Gremaud, R., Broedersz, C. P., Borsa, D. M., Borgschulte, A., Mauron, P., Schreuders, H., Rector, J. H., Dam, B., & Griessen, R. (2007). Hydrogenography: An optical

combinatorial method to find new light-weight hydrogen-storage materials. *Advanced Materials, 19*(19), 2813–2817. https://doi.org/10.1002/adma.200602560

Griessen, R., & Feenstra, R. (1985). Volume changes during hydrogen absorption in metals. *Journal of Physics F: Metal Physics, 15*(4), 1013–1019. https://doi.org/10.1088/0305-4608/15/4/024

Griessen, R., Strohfeldt, N., & Giessen, H. (2016). Thermodynamics of the hybrid interaction of hydrogen with palladium nanoparticles. *Nature Materials, 15*(3), 311–317. https://doi.org/10.1038/nmat4480

Hübert, T., Boon-Brett, L., Black, G., & Banach, U. (2011). Hydrogen sensors – a review. *Sensors and Actuators B: Chemical, 157*(2), 329–352. https://doi.org/10.1016/j.snb.2011.04.070

Hübert, T., Boon-Brett, L., & Buttner, W. (2018). *Sensors for safety and process control in hydrogen technologies*. CRC Press.

Hadjixenophontos, E., Roussel, M., Sato, T., Weigel, A., Stender, P., Orimo, S.i., & Schmitz, G. (2017). Imaging the hydrogenation of Mg thin films. *International Journal of Hydrogen Energy, 42*(35), 22411–22416. https://doi.org/10.1016/j.ijhydene.2017.04.010

Hamm, M., Burlaka, V., Wagner, S., & Pundt, A. (2015). Achieving reversibility of ultra-high mechanical stress by hydrogen loading of thin films. *Applied Physics Letters*, (24), 106. https://doi.org/10.1063/1.4922285

Harumoto, T., Suzuki, Y., Shi, J., & Nakamura, Y. (2017). X-Ray diffraction study on a (111)-textured palladium thin film under hydrogen loading and unloading: Film structure evolution and its mechanism. *Journal of Applied Crystallography, 50*(5), 1478–1489. https://doi.org/10.1107/s1600576717012638

Hitam, C. N. C., Aziz, M. A. A., Ruhaimi, A. H., & Taib, M. R. (2021). Magnesium-based alloys for solid-state hydrogen storage applications: A review. *International Journal of Hydrogen Energy, 46*(60), 31067–31083. https://doi.org/10.1016/j.ijhydene.2021.03.153

Hjörvarsson, B., Rydén, J., Karlsson, E., Birch, J., & Sundgren, J.-E. (1991). Interface effects of hydrogen uptake in Mo/V single-crystal superlattices. *Physical Review B, 43*(8), 6440–6445. https://doi.org/10.1103/physrevb.43.6440

Hong, J., Lee, S., Seo, J., Pyo, S., Kim, J., & Lee, T. (2015). A highly sensitive hydrogen sensor with gas selectivity using a PMMA membrane-coated Pd nanoparticle/single-layer graphene hybrid. *ACS Applied Materials and Interfaces, 7*(6), 3554–3561. https://doi.org/10.1021/am5073645

Hosoki, A., Nishiyama, M., Igawa, H., Seki, A., Choi, Y., & Watanabe, K. (2013). A surface plasmon resonance hydrogen sensor using Au/Ta_2O_5/Pd multi-layers on hetero-core optical fiber structures. *Sensors and Actuators B: Chemical, 185*, 53–58. https://doi.org/10.1016/j.snb.2013.04.072

Hughes, R. C., Schubert, W. K., & Buss, R. J. (1995). Solid-state hydrogen sensors using palladium-nickel alloys: Effect of alloy composition on sensor response. *Journal of the Electrochemical Society, 142*(1), 249–254. https://doi.org/10.1149/1.2043887

Huiberts, J. N., Griessen, R., Rector, J. H., Wijngaarden, R. J., Dekker, J. P., de Groot, D. G., & Koeman, N. J. (1996). Yttrium and lanthanum hydride films with switchable optical properties. *Nature, 380*(6571), 231–234. https://doi.org/10.1038/380231a0

Huiberts, J. N., Griessen, R., Wijngaarden, R. J., Kremers, M., & Van Haesendonck, C. (1997). Logarithmic divergence of the electrical resistivity in the metal hydride $YH_{3-\delta}$. *Physical Review Letters, 79*(19), 3724–3727. https://doi.org/10.1103/physrevlett.79.3724

Kerssemakers, J. W. J., van der Molen, S. J., Günther, R., Dam, B., & Griessen, R. (2002). Local switching in epitaxial YH_x switchable mirrors. *Physical Review B, 65*(7). https://doi.org/10.1103/physrevb.65.075417

Kim, H. M., Kim, H. J., Yang, S. C., Park, J. H., & Lee, S. K. (2022). Fiber optic localized surface plasmon resonance hydrogen sensor based on gold nanoparticles capped with palladium. *Journal of Industrial and Engineering Chemistry, 111*, 281–288. https://doi.org/10.1016/j.jiec.2022.04.008

Koo, W. T., Cho, H. J., Kim, D. H., Kim, Y. H., Shin, H., Penner, R. M., & Kim, I. D. (2020). Chemiresistive hydrogen sensors: Fundamentals, recent advances, and challenges. *ACS Nano, 14*(11), 14284–14322. https://doi.org/10.1021/acsnano.0c05307

Lakshmanan, S., & Bhati, M. (2024). Unravelling the atmospheric and climate implications of hydrogen leakage. *International Journal of Hydrogen Energy, 53*, 807–815. https://doi.org/10.1016/j.ijhydene.2023.12.010

Laudahn, U., Fähler, S., Krebs, H. U., Pundt, A., Bicker, M., Hülsen, U.v., Geyer, U., & Kirchheim, R. (1999). Determination of elastic constants in thin films using hydrogen loading. *Applied Physics Letters, 74*(5), 647–649. https://doi.org/10.1063/1.123028

Lee, E., Lee, J. M., Lee, E., Noh, J. S., Joe, J. H., Jung, B., & Lee, W. (2010). Hydrogen gas sensing performance of Pd-Ni alloy thin films. *Thin Solid Films, 519*(2), 880–884. https://doi.org/10.1016/j.tsf.2010.07.122

Lewis, F. A. (1982). The palladium-hydrogen system. *Platinum Metals Review, 26*(1), 20–27. https://doi.org/10.1595/003214082x2612027

Li, Q., Lu, Y., Luo, Q., Yang, X., Yang, Y., Tan, J., … Pan, F. (2021). Thermodynamics and kinetics of hydriding and dehydriding reactions in Mg-based hydrogen storage materials. *Journal of Magnesium and Alloys, 9*(6), 1922–1941. https://doi.org/10.1016/j.jma.2021.10.002

Liang, R., Liu, D., Sun, Y., Luo, X., Grant, D., Walker, G., & Wu, Y. (2019). Investigation of Mg-Y coated gasochromic smart windows for building applications. *Building Simulation, 12*(1), 99–112. https://doi.org/10.1007/s12273-018-0483-3

Lin, H. J., Lu, Y. S., Zhang, L. T., Liu, H. Z., Edalati, K., & Révész, Á. (2022). Recent advances in metastable alloys for hydrogen storage: A review. *China Rare Metals, 41*(6), 1797–1817. https://doi.org/10.1007/s12598-021-01917-8

Liu, Y., Chen, J., Peng, L., Deng, N., & Ding, W. (2019). Fabrication and optical property improvement of gasochromic switchable mirror based on Pd/Mg Nb_2O_5 thin film. *International Journal of Hydrogen Energy, 44*(29), 15205–15217. https://doi.org/10.1016/j.ijhydene.2019.04.099

Liu, Y., Chen, J., Peng, L., Han, J., Deng, N., Ding, W., & Chen, W. (2018). Improved optical properties of switchable mirrors based on Pd/Mg-TiO_2 films fabricated by magnetron sputtering. *Materials and Design, 144*, 256–262. https://doi.org/10.1016/j.matdes.2018.02.023

Lokhorst, A. C., Heijna, M. C. R., Rector, J. H., Giebels, I. A. M. E., Koeman, N. J., & Dam, B. (2003). The properties of pulsed laser deposited YH_2 films for switchable devices. *Journal of Alloys and Compounds, 356–357*, 536–540. https://doi.org/10.1016/s0925-8388(03)00118-x

Lu, Y., Asano, K., Schreuders, H., Kim, H., Sakaki, K., Machida, A., Watanuki, T., & Dam, B. (2021). Nanostructural perspective for destabilization of Mg hydride using the immiscible transition metal Mn. *Inorganic Chemistry, 60*(19), 15024–15030. https://doi.org/10.1021/acs.inorgchem.1c02525

Lu, Y., Kim, H., Sakaki, K., Hayashi, S., Jimura, K., & Asano, K. (2019). Destabilizing the dehydrogenation thermodynamics of magnesium hydride by utilizing the immiscibility of Mn with Mg. *Inorganic Chemistry, 58*(21), 14600–14607. https://doi.org/10.1021/acs.inorgchem.9b02253

Luong, H. M., Pham, M. T., Guin, T., Madhogaria, R. P., Phan, M. H., Larsen, G. K., & Nguyen, T. D. (2021). Sub-second and ppm-level optical sensing of hydrogen using templated control of nano-hydride geometry and composition. *Nature Research, United States Nature Communications, 12*(1). https://doi.org/10.1038/s41467-021-22697-w

Ma, B., Yang, P., Jiang, C., Pan, Q., & Chen, C. (2023). Wafer-scale hysteresis-free plasmonic hydrogen sensors based on Pd–Au alloy nanoarrays. *International Journal of Hydrogen Energy. 03603199, 48*(80), 31392–31399. https://doi.org/10.1016/j.ijhydene.2023.04.245

Maiorov, V. A. (2020). Metal hydride switchable mirrors. *Optics and Spectroscopy, 128*(1), 148–165. https://doi.org/10.1134/s0030400x20010154

Manchester, F. D., San-Martin, A., & Pitre, J. M. (1994). The H-Pd (hydrogen-palladium) System. *Journal of Phase Equilibria, 15*(1), 62–83. https://doi.org/10.1007/bf02667685

Mintz, M. H. (1996). Hafnium-hydrogen. *Solid State Phenomena*, 331–356. https://doi.org/10.1007/BF02667685

Moehlecke, S., Majkrzak, C. F., & Strongin, M. (1985). Enhanced hydrogen solubility in niobium films. *Physical Review B, 31*(10), 6804–6806. https://doi.org/10.1103/physrevb.31.6804

Mooij, L. P. A., Baldi, A., Boelsma, C., Shen, K., Wagemaker, M., Pivak, Y., Schreuders, H., Griessen, R., & Dam, B. (2011). Interface energy controlled thermodynamics of nanoscale metal hydrides. *Advanced Energy Materials, 1*(5), 754–758. https://doi.org/10.1002/aenm.201100316

Mooij, L., & Dam, B. (2013). Nucleation and growth mechanisms of nano magnesium hydride from the hydrogen sorption kinetics. *Physical Chemistry Chemical Physics, 15*(27), 11501–11510. https://doi.org/10.1039/c3cp51735g

Nagengast, D. G., van Gogh, A. T. M., Kooij, E. S., Dam, B., & Griessen, R. (1999). Contrast enhancement of rare-earth switchable mirrors through microscopic shutter effect. *Applied Physics Letters, 75*(14), 2050–2052. https://doi.org/10.1063/1.124912

Namba, K., Ogura, S., Ohno, S., Wen, Di, Kato, K., Wilde, M., Pletikosić, I., Pervan, P., Milun, M., & Fukutani, K. (2018). Acceleration of hydrogen absorption by palladium through surface alloying with gold. *Proceedings of the National Academy of Sciences, 115*(31), 7896–7900. https://doi.org/10.1073/pnas.1800412115

Nelson, A. (2006). Co-refinement of multiple-contrast neutron/X-ray reflectivity data using MOTOFIT. *Journal of Applied Crystallography, 39*(2), 273–276. https://doi.org/10.1107/s0021889806005073

Ng, K. K., Zhang, F. C., Anisimov, V. I., & Rice, T. M. (1997). Electronic structure of lanthanum hydrides with switchable optical properties. *Physical Review Letters, 78*(7), 1311–1314. https://doi.org/10.1103/physrevlett.78.1311

Ng, K. K., Zhang, F. C., Anisimov, V. I., & Rice, T. M. (1999). Theory for metal hydrides with switchable optical properties. *Physical Review B, 59*(8), 5398–5413. https://doi.org/10.1103/physrevb.59.5398

Ngene, P., Longo, A., Mooij, L., Bras, W., & Dam, B. (2017). Metal-hydrogen systems with an exceptionally large and tunable thermodynamic destabilization. *Nature Communications, 8*(1). https://doi.org/10.1038/s41467-017-02043-9

Ngene, P., Radeva, T., Slaman, M., Westerwaal, R. J., Schreuders, H., & Dam, B. (2014). Seeing hydrogen in colors: Low-cost and highly sensitive eye readable hydrogen detectors. *Advanced Functional Materials, 24*(16), 2374–2382. https://doi.org/10.1002/adfm.201303065

Ngene, P., Westerwaal, R. J., Sachdeva, S., Haije, W., de Smet, L. C. P. M., & Dam, B. (2014). Polymer-induced surface modifications of Pd-based thin films leading to improved

kinetics in hydrogen sensing and energy storage applications. *Angewandte Chemie International Edition, 53*(45), 12081–12085. https://doi.org/10.1002/anie.201406911

Nicolas, M., Dumoulin, L., & Burger, J. P. (1986). Thickness dependence of the critical solution temperature of hydrogen in Pd films. *Journal of Applied Physics, 60*(9), 3125–3130. https://doi.org/10.1063/1.337724

Nix, W. D. (1989). Mechanical properties of thin films. *Metallurgical Transactions A, 20*(11), 2217–2245. https://doi.org/10.1007/BF02666659

Nugroho, F. A. A., Darmadi, I., Cusinato, L., Susarrey-Arce, A., Schreuders, H., Bannenberg, L. J., da Silva Fanta, A. B., Kadkhodazadeh, S., Wagner, J. B., Antosiewicz, T. J., Hellman, A., Zhdanov, V. P., Dam, B., & Langhammer, C. (2019). Metal–polymer hybrid nanomaterials for plasmonic ultrafast hydrogen detection. *Nature Materials, 18*(5), 489–495. https://doi.org/10.1038/s41563-019-0325-4

Nugroho, F. A. A., Darmadi, I., Zhdanov, V. P., & Langhammer, C. (2018). Universal scaling and design rules of hydrogen-induced optical properties in Pd and Pd-alloy nanoparticles. *ACS Nano, 12*(10), 9903–9912. https://doi.org/10.1021/acsnano.8b02835

Nugroho, F. A. A., Eklund, R., Nilsson, S., & Langhammer, C. (2018). A fiber-optic nanoplasmonic hydrogen sensor: Via pattern-transfer of nanofabricated PdAu alloy nanostructures. *Royal Society of Chemistry, Sweden Nanoscale, 10*(44), 20533–20539. https://doi.org/10.1039/c8nr03751e

Ocko, I. B., & Hamburg, S. P. (2022). Climate consequences of hydrogen emissions. *Atmospheric Chemistry and Physics, 22*(14), 9349–9368. https://doi.org/10.5194/acp-22-9349-2022

Oliveira, A. M., Beswick, R. R., & Yan, Y. (2021). A green hydrogen economy for a renewable energy society. *Current Opinion in Chemical Engineering, 33*. https://doi.org/10.1016/j.coche.2021.100701

Olsson, S. (2002). HH interactions in Nb/W (110) superlattices. *Physical Review B, 66*(15). https://doi.org/10.1103/PhysRevB.66.155433

Ouyang, L., Liu, F., Wang, H., Liu, J., Yang, X.-S., Sun, L., & Zhu, M. (2020). Magnesium-based hydrogen storage compounds: A review. *Journal of Alloys and Compounds, 832*. https://doi.org/10.1016/j.jallcom.2020.154865, 09258388.

Palm, K. J., Murray, J. B., McClure, J. P., Leite, M. S., & Munday, J. N. (2019). In situ optical and stress characterization of alloyed Pd_xAu_{1-x} hydrides. *ACS Applied Materials and Interfaces, 11*(48), 45057–45067. https://doi.org/10.1021/acsami.9b14244

Palm, K. J., Murray, J. B., Narayan, T. C., & Munday, J. N. (2018). Dynamic optical properties of metal hydrides. *ACS Photonics, 5*(11), 4677–4686. https://doi.org/10.1021/acsphotonics.8b01243

Palmisano, V., Filippi, M., Baldi, A., Slaman, M., Schreuders, H., & Dam, B. (2010). An optical hydrogen sensor based on a Pd-capped Mg thin film wedge. *International Journal of Hydrogen Energy, 35*(22), 12574–12578. https://doi.org/10.1016/j.ijhydene.2010.09.001

Paudel, B., Dhas, J. A., Zhou, Y., Choi, M. J., Senor, D. J., Chang, C. H., Du, Y., & Zhu, Z. (2024). ToF-SIMS in material research: A view from nanoscale hydrogen detection. *Materials Today, 75*, 149–165. https://doi.org/10.1016/j.mattod.2024.03.003

Pedersen, T. P. L., Liesch, C., Salinga, C., Eleftheriadis, T., Weis, H., & Wuttig, M. (2004). Hydrogen-induced changes of mechanical stress and optical transmission in thin Pd films. *Thin Solid Films, 458*(1–2), 299–303. https://doi.org/10.1016/j.tsf.2003.12.040

Perrotton, C., Westerwaal, R. J., Javahiraly, N., Slaman, M., Schreuders, H., Dam, B., & Meyrueis, P. (2013). A reliable, sensitive and fast optical fiber hydrogen sensor based on surface plasmon resonance. *Optics Express, 21*(1), 382–390. https://doi.org/10.1364/OE.21.000382

Ping, X., Cao, X., Cao, C., Lei, H., Yang, C., Cheng, Q., & Liu, M. (2024). Fiber grating hydrogen sensor: Progress, challenge and prospect. *Advanced Sensor Research, 3*(2), 2300088. https://doi.org/10.1002/adsr.202300088

Pivak, Y., Schreuders, H., Slaman, M., Griessen, R., & Dam, B. (2011). Thermodynamics, stress release and hysteresis behavior in highly adhesive Pd–H films. *International Journal of Hydrogen Energy, 36*(6), 4056–4067. https://doi.org/10.1016/j.ijhydene.2010.12.063

Prinz, J., Pálsson, G. K., Korelis, P. T., & Hjörvarsson, B. (2010). Combined light and electron scattering for exploring hydrogen in thin metallic films. *Applied Physics Letters, 97*(25). https://doi.org/10.1063/1.3529465

Pundt, A., & Kirchheim, R. (2006). Hydrogen in metals: Microstructural aspects. *Annual Review of Materials Research, 36*(1), 555–608. https://doi.org/10.1146/annurev.matsci.36.090804.094451

Radeva, T., Ngene, P., Slaman, M., Westerwaal, R., Schreuders, H., & Dam, B. (2014). Highly sensitive and selective visual hydrogen detectors based on Y_xMg_{1-x} thin films. *Sensors and Actuators B: Chemical. 09254005, 203*, 745–751. https://doi.org/10.1016/j.snb.2014.06.134

Remhof, A., Kerssemakers, J. W. J., van der Molen, S. J., Griessen, R., & Kooij, E. S. (2002). Hysteresis in YH_x films observed with in situ measurements. *Physical Review B, 65*(5), 054110. https://doi.org/10.1103/PhysRevB.65.054110

Remhof, A., & Borgschulte, A. (2008). Thin-film metal hydrides. *ChemPhysChem, 9*(17), 2440–2455. https://doi.org/10.1002/cphc.200800573

Richardson, T. J., Slack, J. L., Armitage, R. D., Kostecki, R., Farangis, B., & Rubin, M. D. (2001). Switchable mirrors based on nickel–magnesium films. *Applied Physics Letters, 78*(20), 3047–3049. https://doi.org/10.1063/1.1371959

Richardson, T. J., Slack, J. L., Farangis, B., & Rubin, M. D. (2002). Mixed metal films with switchable optical properties. *Applied Physics Letters, 80*(8), 1349–1351. https://doi.org/10.1063/1.1454218

Rydén, J., Hjörvarsson, B., Ericsson, T., Karlsson, E., Krozer, A., & Kasemo, B. (1989). Unusual kinetics of hydride formation in Mg•Pd sandwiches, studied by hydrogen profiling and quartz crystal microbalance measurements. *Journal of the Less Common Metals, 152*(2), 295–309. https://doi.org/10.1016/0022-5088(89)90097-0

Salomons, E. M., Feenstra, R., de Groot, D. G., Rector, J. H., & Griessen, R. (1987). Pressure-composition isotherms of thin PdH_c films. *Journal of the Less Common Metals, 130*(C), 415–420. https://doi.org/10.1016/0022-5088(87)90136-6

Sand, M., Skeie, R. B., Sandstad, M., Krishnan, S., Myhre, G., Bryant, H., Derwent, R., Hauglustaine, D., Paulot, F., Prather, M., & Stevenson, D. (2023). A multi-model assessment of the Global Warming Potential of hydrogen. *Communications Earth and Environment, 4*(1). https://doi.org/10.1038/s43247-023-00857-8

Schober, T. (1996). Vanadium-, niobium- and tantalum-hydrogen. *Solid State Phenomena, 49–50*, 357–422. https://doi.org/10.4028/www.scientific.net/SSP.49-50.357

Schwarz, R. B. (1999). Hydrogen storage in magnesium-based alloys. *MRS Bulletin, 24*(11), 40–44. https://doi.org/10.1557/s0883769400053446

Schwarz, R. B., & Khachaturyan, A. G. (2006). Thermodynamics of open two-phase systems with coherent interfaces: Application to metal–hydrogen systems. *Acta Materialia, 54*(2), 313–323. https://doi.org/10.1016/j.actamat.2005.08.044

Sears, V. F. (1992). Neutron scattering lengths and cross sections. *Neutron news, 3*(3), 26–37.

Sharma, B., & Kim, J. S. (2017). Pd/Ag alloy as an application for hydrogen sensing. *International Journal of Hydrogen Energy, 42*(40), 25446–25452. https://doi.org/10.1016/j.ijhydene.2017.08.142

Slaman, M., Dam, B., Pasturel, M., Borsa, D. M., Schreuders, H., Rector, J. H., & Griessen, R. (2007). Fiber optic hydrogen detectors containing Mg-based metal hydrides. *Sensors and Actuators B: Chemical, 123*(1), 538–545. https://doi.org/10.1016/j.snb.2006.09.058

Song, G., Remhof, A., Theis-Bröhl, K., & Zabel, H. (1997). Extraordinary adhesion of niobium on sapphire substrates. *Physical Review Letters, 79*(25), 5062–5065. https://doi.org/10.1103/physrevlett.79.5062

Song, M., Zhang, L., Wu, F., Zhang, H., Zhao, H., Chen, L., & Li, H. (2023). Recent advances of magnesium hydride as an energy storage material. *Journal of Materials Science and Technology, 149*, 99–111. https://doi.org/10.1016/j.jmst.2022.11.032

Soroka, O., Sturm, J. M., Lee, C. J., Schreuders, H., Dam, B., & Bijkerk, F. (2020). Hydrogen diffusion through Ru thin films. *International Journal of Hydrogen Energy, 45*(29), 15003–15010. https://doi.org/10.1016/j.ijhydene.2020.03.201

Sterl, F., Strohfeldt, N., Both, S., Herkert, E., Weiss, T., & Giessen, H. (2020). Design principles for sensitivity optimization in plasmonic hydrogen sensors. *ACS Sensors, 5*(4), 917–927. https://doi.org/10.1021/acssensors.9b02436

Strohfeldt, N., Tittl, A., & Giessen, H. (2013). Long-term stability of capped and buffered palladium-nickel thin films and nanostructures for plasmonic hydrogen sensing applications. *Optical Materials Express, 3*(2), 194–204. https://doi.org/10.1364/OME.3.000194Germany

Syrenova, S., Wadell, C., Nugroho, F. A. A., Gschneidtner, T. A., Diaz Fernandez, Y. A., Nalin, G., ¬witlik, D., Westerlund, F., Antosiewicz, T. J., Zhdanov, V. P., Moth-Poulsen, K., & Langhammer, C. (2015). Hydride formation thermodynamics and hysteresis in individual Pd nanocrystals with different size and shape. *Nature Materials, 14*(12), 1236–1244. https://doi.org/10.1038/nmat4409

Tajima, K., Yamada, Y., Bao, S., Okada, M., & Yoshimura, K. (2008). Near colorless all-solid-state switchable mirror based on magnesium-titanium thin film. *Journal of Applied Physics*, (1), 103. https://doi.org/10.1063/1.2829816

Tajima, K., Yamada, Y., Okada, M., & Yoshimura, K. (2010). Fabrication study of proton injection layer suitable for electrochromic switchable mirror glass. *Thin Solid Films, 519*(2), 934–937. https://doi.org/10.1016/j.tsf.2010.09.021

Tashie-Lewis, B. C., & Nnabuife, S. G. (2021). Hydrogen production, distribution, storage and power conversion in a hydrogen economy - a Technology review. *Chemical Engineering Journal Advances, 8*. https://doi.org/10.1016/j.ceja.2021.100172

Tomeček, D., Moberg, H. K., Nilsson, S., Theodoridis, A., Darmadi, I., Midtvedt, D., Volpe, G., Andersson, O., & Langhammer, C. (2024). Neural network enabled nanoplasmonic hydrogen sensors with 100 ppm limit of detection in humid air. *Nature Communications, 15*(1), Article 20411723. https://doi.org/10.1038/s41467-024-45484-9

Trouillet, A., Marin, E., & Veillas, C. (2006). Fibre gratings for hydrogen sensing. *Measurement Science and Technology, 17*(5), 1124–1128. https://doi.org/10.1088/0957-0233/17/5/s31

Tsakiris, T., Komander, K., Wolff, M., Frost, R. J. W., Droulias, S. A., Pálsson, G. K., & Primetzhofer, D. (2024). Correlation of optical transmittance and hydrogen concentration in Cr/V superlattices. *Nuclear Instruments and Methods in Physics Research, Section B: Beam Interactions with Materials and Atoms, 553*. https://doi.org/10.1016/j.nimb.2024.165398

Uchida, H. T., Kirchheim, R., & Pundt, A. (2011). Influence of hydrogen loading conditions on the blocking effect of nanocrystalline Mg films. *Scripta Materialia, 64*(10), 935–937. https://doi.org/10.1016/j.scriptamat.2011.01.036

Uchida, H. T., Wagner, S., Hamm, M., Kürschner, J., Kirchheim, R., Hjörvarsson, B., & Pundt, A. (2015). Absorption kinetics and hydride formation in magnesium films: Effect of driving force revisited. *Acta Materialia, 85*, 279–289. https://doi.org/10.1016/j.actamat.2014.11.031

Van der Molen, Nagengast, D. G., Van Gogh, Kalkman, J., Kooij, E. S., Rector, J. H., & Griessen, R. (2001). Insulating fcc $YH_{3-\delta}$ stabilized by MgH_2. *Physical Review B, 63*(23), 235116. https://doi.org/10.1103/PhysRevB.63.235116

van der Sluis, P., Ouwerkerk, M., & Duine, P. A. (1997). Optical switches based on magnesium lanthanide alloy hydrides. *Applied Physics Letters, 70*(25), 3356–3358. https://doi.org/10.1063/1.119169

van Gogh, A. T. M., Nagengast, D. G., Kooij, E. S., Koeman, N. J., & Griessen, R. (2000). Quenching of giant hysteresis effects in $La_{1-z}Y_zH_x$ switchable mirrors. *Physical Review Letters, 85*(10), 2156–2159. https://doi.org/10.1103/physrevlett.85.2156

Verhoeff, D. J., Schreuders, H., & Bannenberg, L. J. (2025). Tantalum-palladium alloy based optical micro-mirror hydrogen sensor. *Sensors and Actuators B: Chemical, 428*. https://doi.org/10.1016/j.snb.2025.137229

Vermeulen, P., Ledovskikh, A., Danilov, D., & Notten, P. H. L. (2009). Thermodynamics and kinetics of the thin film magnesium–hydrogen system. *Acta Materialia, 57*(17), 4967–4973. https://doi.org/10.1016/j.actamat.2009.06.058

Victoria, M., Westerwaal, R. J., Dam, B., & Van Mechelen, J. L. M. (2016). Amorphous metal-hydrides for optical hydrogen sensing: The effect of adding glassy Ni-Zr to Mg-Ni-H. *ACS Sensors, 1*(3), 222–226. https://doi.org/10.1021/acssensors.5b00265

Wadell, C., Nugroho, F. A. A., Lidström, E., Iandolo, B., Wagner, J. B., & Langhammer, C. (2015). Hysteresis-free nanoplasmonic pd-au alloy hydrogen sensors. *Nano Letters, 15*(5), 3563–3570. Available from: http://pubs.acs.org/journal/nalefd. doi: 10.1021/acs.nanolett.5b01053.

Wadell, C., Syrenova, S., & Langhammer, C. (2014). Plasmonic hydrogen sensing with nanostructured metal hydrides. *ACS Nano, 8*(12), 11925–11940. https://doi.org/10.1021/nn505804f

Wagner, H., & Horner, H. (1974). Elastic interaction and the phase transition in coherent metal-hydrogen systems. *Advances in Physics, 23*(4), 587–637. https://doi.org/10.1080/00018737400101401

Wagner, S., Klose, P., Burlaka, V., Nörthemann, K., Hamm, M., & Pundt, A. (2019). Structural phase transitions in niobium hydrogen thin films: Mechanical stress, phase equilibria and critical temperatures. *ChemPhysChem, 20*(14), 1890–1904. https://doi.org/10.1002/cphc.201900247

Wagner, S., Kramer, T., Uchida, H., Dobron, P., Cizek, J., & Pundt, A. (2016). Mechanical stress and stress release channels in 10–350 nm palladium hydrogen thin films with different micro-structures. *Acta Materialia, 114*, 116–125. https://doi.org/10.1016/j.actamat.2016.05.023

Wagner, S., & Pundt, A. (2016). Quasi-thermodynamic model on hydride formation in palladium–hydrogen thin films: Impact of elastic and microstructural constraints. *International Journal of Hydrogen Energy, 41*(4), 2727–2738. https://doi.org/10.1016/j.ijhydene.2015.11.063

Wang, M., & Feng, Y. (2007). Palladium–silver thin film for hydrogen sensing. *Sensors and Actuators B: Chemical, 123*(1), 101–106. https://doi.org/10.1016/j.snb.2006.07.030

Westerwaal, R. J., Bouman, E. A., Haije, W. G., Schreuders, H., Dutta, S., Wu, M. Y., Boelsma, C., Ngene, P., Basak, S., & Dam, B. (2015). The hydrogen permeability of Pd–Cu based thin film membranes in relation to their structure: A combinatorial approach.

International Journal of Hydrogen Energy, 40(10), 3932–3943. https://doi.org/10.1016/j.ijhydene.2015.01.124

Westerwaal, R. J., Rooijmans, J. S. A., Leclercq, L., Gheorghe, D. G., Radeva, T., Mooij, L., Mak, T., Polak, L., Slaman, M., Dam, B., & Rasing, T. (2013). Nanostructured Pd–Au based fiber optic sensors for probing hydrogen concentrations in gas mixtures. *International Journal of Hydrogen Energy, 38*(10), 4201–4212. https://doi.org/10.1016/j.ijhydene.2012.12.146

Wicke, E., & Nernst, G. H. (1964). Zustandsdiagramm und thermodynamisches Verhalten der Systeme Pd/H_2 und Pd/D_2 bei normalen Temperaturen; H/D-Trenneffekte. *Berichte der Bunsen-Gesellschaft für Physikalische Chemie, 68*(3), 224–235. https://doi.org/10.1002/bbpc.19640680303

Wilde, M., & Fukutani, K. (2014). Hydrogen detection near surfaces and shallow interfaces with resonant nuclear reaction analysis. *Surface Science Reports, 69*(4), 196–295. https://doi.org/10.1016/j.surfrep.2014.08.002

Wolf, W., & Herzig, P. (2002). First-principles investigations for YH_3 (YD_3): Energetics, electric-field gradients, and optical properties. *Physical Review B - Condensed Matter and Materials Physics, 66*(22), 2241121–2241129. https://doi.org/10.1103/PhysRevB.66.224112

Wolf, W., & Herzig, P. (2003). Energetics, electric-field gradients and optical properties of YH_3 (YD_3) by first-principles calculations. *Journal of Alloys and Compounds*, 73–79. https://doi.org/10.1016/s0925-8388(03)00103-8

Xin, X., Johansson, R., Wolff, M., & Hjörvarsson, B. (2016). Hydrogen in vanadium: Site occupancy and isotope effects. *Physical Review B, 93*(13), 134107.

Xin, X., Pálsson, G. K., Wolff, M., & Hjörvarsson, B. (2014). Finite-size effects: Hydrogen in Fe/v (001) superlattices. *Physical Review Letters, 113*(4). https://doi.org/10.1103/PhysRevLett.113.046103

Yamada, Y., Bao, S., Tajima, K., Okada, M., & Yoshimura, K. (2009). Optical properties of switchable mirrors based on magnesium-calcium alloy thin films. *Applied Physics Letters, 94*(19). https://doi.org/10.1063/1.3138130

Yamada, Y., Miura, M., Tajima, K., Okada, M., & Yoshimura, K. (2014). Influence on optical properties and switching durability by introducing Ta intermediate layer in Mg–Y switchable mirrors. *Solar Energy Materials and Solar Cells, 125*, 133–137. https://doi.org/10.1016/j.solmat.2014.02.031

Yamada, Y., Sasaki, H., Tajima, K., Okada, M., & Yoshimura, K. (2012). Optical switching properties of switchable mirrors based on Mg alloyed with alkaline-earth metals. *Solar Energy Materials and Solar Cells, 99*, 73–75. https://doi.org/10.1016/j.solmat.2011.04.016

Yang, F., Kung, S. C., Cheng, M., Hemminger, J. C., & Penner, R. M. (2010). Smaller is faster and more sensitive: The effect of wire size on the detection of hydrogen by single palladium nanowires. *ACS Nano, 4*(9), 5233–5244. https://doi.org/10.1021/nn101475c

Yartys, V. A., Lototskyy, M. V., Akiba, E., Albert, R., Antonov, V. E., Ares, J. R., Baricco, M., Bourgeois, N., Buckley, C. E., Bellosta von Colbe, J. M., Crivello, J.-C., Cuevas, F., Denys, R. V., Dornheim, M., Felderhoff, M., Grant, D. M., Hauback, B. C., Humphries, T. D., Jacob, I., … Zhu, M. (2019). Magnesium based materials for hydrogen based energy storage: Past, present and future. *International Journal of Hydrogen Energy, 44*(15), 7809–7859. https://doi.org/10.1016/j.ijhydene.2018.12.212

Yoshimura, K., Bao, S., Uchiyama, N., Matsumoto, H., Kanai, T., Nakabayashi, S., & Kanayama, H. (2008). New hydrogen sensor based on sputtered Mg–Ni alloy thin film. *Vacuum, 83*(3), 699–702. https://doi.org/10.1016/j.vacuum.2008.04.047

Yoshimura, K., Yamada, Y., Bao, S., Tajima, K., & Okada, M. (2007). Degradation of switchable mirror based on Mg–Ni alloy thin film. *Japanese Journal of Applied Physics, 46*(7R), 4260. https://doi.org/10.1143/jjap.46.4260

Yuan, Z., Schreuders, H., Dankelman, R., Dam, B., & Bannenberg, L. J. (2025). Optical hydrogen sensing materials for applications at sub-zero temperatures. *Advanced Functional Materials, 35*(23). https://doi.org/10.1002/adfm.202420087

Zabel, H., & Peisl, H. (1979). Sample-shape-dependent phase transition of hydrogen in niobium. *Physical Review Letters, 42*(8), 511–514. https://doi.org/10.1103/physrevlett.42.511

Zabel, H., & Peisl, H. (1980). Coherent α-α′ phase transition of hydrogen in niobium. *Acta Metallurgica, 28*(5), 589–599. https://doi.org/10.1016/0001-6160(80)90125-x

Zahiri, B., Amirkhiz, B. S., Danaie, M., & Mitlin, D. (2010). Bimetallic Fe-V catalyzed magnesium films exhibiting rapid and cycleable hydrogenation at 200 °C. *Applied Physics Letters, 96*(1). https://doi.org/10.1063/1.3275864

Zaluska, A., Zaluski, L., & Ström–Olsen, J. O. (1999). Nanocrystalline magnesium for hydrogen storage. *Journal of Alloys and Compounds, 288*(1–2), 217–225. https://doi.org/10.1016/s0925-8388(99)00073-0

Zhang, Y.n., Peng, H., Qian, X., Zhang, Y., An, G., & Zhao, Y. (2017). Recent advancements in optical fiber hydrogen sensors. *Sensors and Actuators, B: Chemical, 244*, 393–416. https://doi.org/10.1016/j.snb.2017.01.004

Zhang, C., Shen, C., Liu, X., Liu, S., Chen, H., Huang, Z., Wang, Z., Lang, T., Zhao, C., & Zhang, Y. (2022). Pd/Au nanofilms based tilted fiber Bragg grating hydrogen sensor. *Optics Communications, 502*. https://doi.org/10.1016/j.optcom.2021.127424

Zhdanov, V. P., Krozer, A., & Kasemo, B. (1993). Kinetics of first-order phase transitions initiated by diffusion of particles from the surface into the bulk. *Physical Review B, 47*(17), 11044–11048. https://doi.org/10.1103/physrevb.47.11044

Zhou, C., Fang, Z. Z., Lu, J., Luo, X., Ren, C., Fan, P., Ren, Y., & Zhang, X. (2014). Thermodynamic destabilization of magnesium hydride using Mg-based solid solution alloys. *Journal of Physical Chemistry C, 118*(22), 11526–11535. https://doi.org/10.1021/jp501306w